IEEE TRANSACTIONS ON POWER ELECTRONICS, VOL. 35, NO. 5, MAY 2020 5479

Output Impedance Modeling of Single-Phase Grid-Tied Inverters With Capturing the Frequency-Coupling Effect of PLL

Qiang Qian, *Student Member, IEEE*, Shaojun Xie, *Member, IEEE*, Jinming Xu, *Member, IEEE*,
Kunshan Xu, *Member, IEEE*, Shenyiyang Bian, and Nini Zhong

***Abstract*—The output impedance model for the precise stability analysis on the single-phase grid-tied inverters considering the frequency-coupling effect of the phase-locked loop (PLL) is studied. A multifrequency admittance matrix (MAM) is developed to predict the inverter-grid system stability by applying the generalized Nyquist criterion. Based on the MAM, a novel output impedance model characterized by clear physical meaning is proposed, which reveals that the inverter output impedance ($Z_{op}|_{(Z_{\text{pcc}},I_m)}$) varies along with the grid impedance Z_{pcc} and the current reference I_m. The resonance and the stability problems can be identified by applying the impedance-based stability criterion to the impedance ratio $Z_{op}|_{(Z_{\text{pcc}},\,I_m)}/Z_{\text{pcc}}$. The proposed impedance model is further extended to the *n*-parallel inverter system. It is found that the output impedances of two *n*-parallel homogeneous-inverter systems are identical if the number *n* and the total injected current i_{tot} are the same, and the system stability is indicated by the impedance ratio $\frac{1}{n}\,Z_{op}|_{(n\cdot Z_{\text{pcc}},\,I_{\text{avg}})}/Z_{\text{pcc}}$, where $Z_{op}|_{(n\cdot Z_{\text{pcc}},\,I_{\text{avg}})}$ is the output impedance of one special inverter with the average current i_{tot}/n injected to the grid with $n\cdot Z_{\text{pcc}}$. Further on, the design procedure of the PLL bandwidth f_b is elaborated, which guides the selection of f_b with the anticipated phase margin. Compared to the conventional impedance model, the developed output impedance is more qualified to precisely identify the harmonic stability problem in the weak grid. The selection of f_b and the correctness of the proposed impedance model are experimentally verified by the measured output impedance and the waveforms of the elaborated cases.**

***Index Terms*—Frequency-coupling effect, grid-tied inverters, harmonic, output impedance, phase-locked loop (PLL).**

I. INTRODUCTION

IN THE distributed power generation system, grid-tied inverters play a key role in bridging the renewable energy resource and the grid [1]. The dynamic interactions between the inverters and the grid may arouse the harmonic stability problem, which has drawn much attention in the last decade. It has been shown that due to the presence of the grid impedance, harmonics may be excited at the point of the common coupling (PCC) over a wide frequency band, ranging from the grid synchronization loop (sub and super synchronous frequencies) to the inner current control loop (hundreds of Hz to kHz) [2].

To address the resonance challenges in inverter-grid systems, modeling and control methods have been performed for characterizing and damping the resonances. Although great efforts have been made to improve the stability of the inner current control with the digital control delay taken into account [3], [4], less attention has been drawn to the low-frequency resonance issues caused by the grid synchronization when the grid impedance is nonnegligible [5]–[10].

In either single-phase or three-phase application, the synchronous reference frame phase-locked loop (SRF-PLL) has been widely adopted to keep the phase of the grid current synchronized with that of the PCC voltage [6]–[15]. The phase-locked loop (PLL) bandwidth is adaptively selected (typically larger than 30 Hz) to realize a trade-off design between the fast PLL dynamic response and the stability in [6]. Moreover, considering the low-voltage grid faults, the proper injection of the reactive current is required to be activated within 20 ms [16], which limits the settling time of the PLL loop to accomplish the correct synchronization with the faulted grid [12]. In other words, the high PLL bandwidth is expected to guarantee the capability of the low-voltage ride through [13]–[15]. Hence, the dynamic response of the inverter may be influenced by the PLL over a wide frequency band [6]. Therefore, there is a need to model the grid-tied inverter with the PLL effect taken into account. However, after performing the coordinate transformation, the *q*-axis component of the PCC voltage is obtained and regulated for the phase tracking. The nonlinear trigonometric functions inside the SRF-PLL result in the frequency coupling effect (FCE) [17]–[20], which complicates the frequency components in the current reference and adds significant complexity to the modeling of the inverter.

At present, most works are focused on the impedance modeling of PLL in the three-phase inverter-grid system, which can be categorized into two impedance equivalents. The first impedance model is developed in the rotating *dq*-frame, which relates the *d* and *q* axis PCC voltage to the corresponding grid

---

Manuscript received March 18, 2019; revised June 15, 2019 and August 24, 2019; accepted October 7, 2019. Date of publication October 10, 2019; date of current version February 11, 2020. This work was supported in part by the National Natural Science Foundation of China under Grant 51877104, in part by the National Natural Science Foundation of China under Grant 51807089, and in part by the Natural Science Foundation of Jiangsu Province under Grant BK20180432. Recommended for publication by Associate Editor J. M. Alonso. *(Corresponding author: Shaojun Xie.)*

The authors are with the College of Automation Engineering, Nanjing University of Aeronautics and Astronautics, Nanjing 211106, China (e-mail: nuaaqianqiang@nuaa.edu.cn; eeac@nuaa.edu.cn; xjinming01@163.com; xks1986@163.com; shenyiyangbian@163.com; ZhongNnqc@163.com).

Color versions of one or more of the figures in this article are available online at http://ieeexplore.ieee.org.

Digital Object Identifier 10.1109/TPEL.2019.2946984

current [8], [9], [19]. Although the resulting 2×2 off-diagonal impedance matrix is qualified for revealing the stability impact of the SRF-PLL, it has the limitations in analyzing the dynamic interactions between the inverter and the grid, especially in perceiving the FCE [20]. The second approach applies the harmonic linearization method in the stationary $\alpha\beta$-frame through symmetric components, yielding the sequence-domain or the phase-domain impedance model [20]–[25]. Since the sequence-domain model reduces the model to a diagonal impedance matrix by neglecting the FCE, the system stability can be predicted by directly applying the traditional impedance-based stability criterion (ISC) [26]. Compared with the *dq*-frame model, the analysis may be simpler, but more inaccurate and ambiguous. The discrepancy between the two models on the stability estimation can be found in [20] and [21]. In order to obtain the same stability predictions as the *dq*-frame model implies, a modified sequence-domain model is proposed in [23] to capture the FCE by introducing the transformation matrix, which is similar to the multifrequency impedance model built in [24]. The frequency translations among the models in different domains are further mathematically unveiled by the unified impedance model in [25].

As the inverse Park transformation in the three-phase system is replaced by only the cosine operator in single-phase system, the abovementioned impedance models, including PLL, cannot be applied to the single-phase application. Therefore, Chen *et al.* [27] developed a linearized impedance model by perturbing the orthogonal signals, which were the input of the SRF-PLL. Zhang *et al.* [28] compared the characteristics of the single-phase inverter output impedance with different PLL structures, such as the T/4-delay-based PLL, and the second-order generalized integrator (SOGI) PLL. Although the influences of the SRF-PLL can be analyzed based on the impedance model in [27] and [28] to some extent, these state-of-the-art impedance models for single-phase inverters neglect the FCE, which is reported to be quite different from that in the three-phase system. Specifically, the harmonic at the frequency ω is coupled with that at $\omega \pm 2\omega_0$ in the single-phase inverter [29], [30]. However, the closed-loop analysis of the system is missing, and the interactions between the FCE and the grid impedance are overlooked.

To explicitly reveal the influence of the FCE on the single-phase inverter-grid system stability, the impedance model concerning the FCE of the PLL is established in this article. Salient contributions are summarized as follows.

1) A 3×3 MAM model with capturing the FCE is first proposed based on the multifrequency principle. The system stability can be exactly predicted by applying the generalized Nyquist stability criterion (GNC) to the impedance ratio.
2) Based on the MAM, a single-frequency inverter output impedance, which can be measured by experiments is proposed. It is illustrated that the inverter output impedance depends not only on the inverter itself, but also on the grid impedance. Although this phenomenon is counter intuitive, it is important for exactly identifying the low-order harmonic couplings through the impedance ratio when the weak grid is connected.

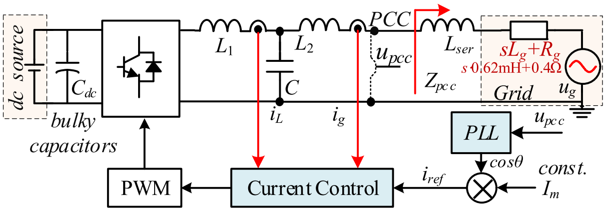

Fig. 1. Illustration of the single-phase grid-tied inverter in weak grid.

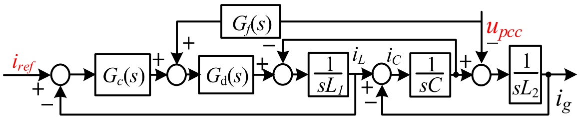

Fig. 2. Control diagram of the inverter-current control.

3) The impedance model is extended to the *n*-parallel inverter system. The output impedances of two *n*-parallel homogeneous-inverter systems are identical if the number and the total grid current i_{tot} are the same. The parallel system stability relies on the impedance ratio $\frac{1}{n}\, Z_{op}|_{(n\cdot Z_{\text{pcc}},\, I_{\text{avg}})}/Z_{\text{pcc}}$, where $Z_{op}|_{(n\cdot Z_{\text{pcc}},\, I_{\text{avg}})}$ is the output impedance of one special inverter with the average current i_{tot}/n injected to the grid with $n \cdot Z_{\text{pcc}}$.
4) The design procedure of the PLL bandwidth is elaborated, which ensures the inverter-grid system stability with the anticipated phase margin (PM).

II. General Impedance Model Concerning the PLL

A. System Description

Fig. 1 shows the general configuration of a single-phase *LCL*-filtered grid-tied inverter, which is assumed to be decoupled with the constant dc voltage source because of the bulky dc capacitors. Therefore, the dc dynamics are quite slow and are reasonably neglected [12], which is also practically reasonable when the interested frequency band of the PLL is relatively higher than the low bandwidth of the dc voltage regulation loop in the inverter (typically lower than 20 Hz) [30], [31]. The inverter-side inductor L_1, the capacitor *C*, and the grid-side inductor L_2 constitute the *LCL*-filter. The weak grid with an impedance Z_g (i.e., $sL_g + R_g$), which is experimentally measured as s·0.62 mH + 0.4 Ω is considered. The impedance seen from the PCC (Z_{pcc}) is made up of the grid impedance Z_g and the series inductor L_{ser}, which is intensively inserted to simulate different PCC impedance Z_{pcc}.

Various current control methods are feasible for controlling the grid current. The classical inverter-current control shown in Fig. 2 is taken as the analytical example without loss of the generality. In Fig. 2, G_c is the proportional-integral (PI) current regulator, G_f is the PCC voltage feedforward, and G_d is the digital control delay, including the computation and the PWM delay. When the symmetrical regular sampling method is adopted, the one-period delay G_d can be deduced as

$$G_d = T_s^{-1} \cdot e^{-0.5T_c s} \cdot \left(1 - e^{-T_c s}\right)/s \approx e^{-T_c s} \qquad (1)$$

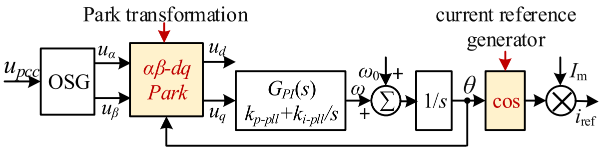

Fig. 3. Control block of the SRF-PLL.

where T_c is the control period. (The Laplace operator "s" is omitted for simplification in the following transfer function).

B. Conventional Single-Frequency Impedance Modeling

Fig. 3 draws the control block of the SRF-PLL. The orthogonal signal can be generated by the T/4-delay PLL, the SOGI-PLL, or other methods. After applying the nonlinear Park transformation to the orthogonal signal of the PCC voltage u_{pcc}, the q-axis voltage u_q is obtained and sent to the input of the PI regulator G_{PI} for generating the phase reference θ. The nonlinear trigonometric functions inside the Park transformation and the current reference generator complicate the modeling of the SRF-PLL. By perturbing the variables in the time-domain equations, the linearized small-signal model of SRF-PLL can be derived as

$$\begin{cases} \tilde{u}_q = -\tilde{\theta} U_m - \sin\theta_0 \cdot \tilde{u}_\alpha + \cos\theta_0 \cdot \tilde{u}_\beta \\ \tilde{\theta} = \int \tilde{\omega} dt = \int (k_{p-\text{pll}} + k_{i-\text{pll}} \int) \tilde{u}_q dt \\ \tilde{i}_{\text{ref}} = -I_m \sin\theta_0 \cdot \tilde{\theta} \end{cases} \tag{2}$$

where the superscript "∼" denotes the perturbation, U_m is the magnitude of the PCC voltage in the $\alpha\beta$ frame (i.e., u_α and u_β), and I_m is the magnitude of the current reference i_{ref}.

By applying the Laplace transform to (1), the small-signal model of SRF-PLL in the s-domain can be described by (3)–(5).

$$\begin{aligned} \tilde{u}_q(s) = & -\tilde{\theta}(s) U_m + 0.5 \cdot [j\tilde{u}_\alpha(s - j\omega_0) - j\tilde{u}_\alpha(s + j\omega_0)] \\ & + 0.5 \cdot [\tilde{u}_\beta(s - j\omega_0) + \tilde{u}_\beta(s + j\omega_0)] \end{aligned} \tag{3}$$

$$\tilde{\theta}(s) = G_{PI}(s) \cdot \tilde{u}_q(s)/s \tag{4}$$

$$\tilde{i}_{\text{ref}}(s) = 0.5 j I_m \left[\tilde{\theta}(s - j\omega_0) - \tilde{\theta}(s + j\omega_0)\right]. \tag{5}$$

By assuming that $\tilde{u}_\alpha = j\tilde{u}_\beta$ and neglecting the FCE, the transfer function from the PCC voltage $\tilde{u}_{\text{pcc}}$ to the current reference $\tilde{i}_{\text{ref}}(T_{\text{pll}})$ can be readily established as

$$\tilde{i}_{\text{ref}} = T_{\text{pll}} \tilde{u}_{\text{pcc}} = I_m H_{\text{pll}} \tilde{u}_{\text{pcc}} = I_m 0.5 G_{\text{pll}}(s - j\omega_0) G_{osg\alpha} \tilde{u}_{\text{pcc}} \tag{6}$$

where $G_{osg\alpha}(s)$ is defined as the transfer function from $\tilde{u}_{\text{pcc}}$ to $\tilde{u}_\alpha$, $H_{\text{pll}}(s)$ is denoted as the transfer function from $\tilde{u}_{\text{pcc}}$ to $\tilde{i}_{\text{ref}}$ with 1-A current reference amplitude, and $G_{\text{pll}}(s)$ is described by

$$G_{\text{pll}}(s - j\omega_0) = \frac{G_{PI}(s - j\omega_0)}{s + U_m G_{PI}(s - j\omega_0)}. \tag{7}$$

Therefore, to incorporate the effect of PLL into the impedance model, the control diagram is modified as Fig. 4, where G_{plant} is the transfer function from i_{ref} to i_g with only the i_L control, and $Y_{\text{inv}-o}$ is the output admittance without the PLL effect. The equivalent admittance of the PLL is denoted as Y_{pll}. The expressions of G_{plant}, $Y_{\text{inv}-o}$, and Y_{pll} are provided as

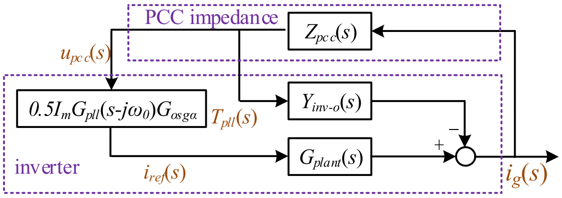

Fig. 4. Modified control diagram including the PLL effect.

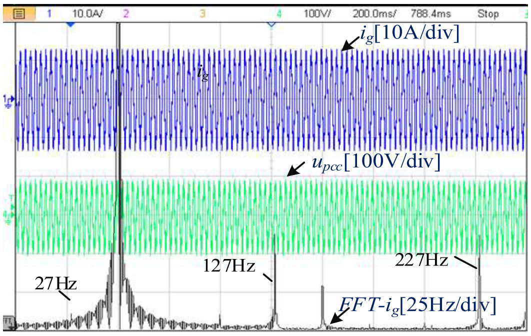

Fig. 5. Illustration of the FCE phenomenon when the PCC voltage is perturbed at the frequency 127 Hz.

$$\begin{aligned} G_{\text{plant}} &= G_c G_d / \left(s^3 L_1 L_2 C + G_c G_d s^2 L_2 C + s L_1 + s L_2\right) \\ &= G_c G_d / \Delta \end{aligned} \tag{8}$$

$$Y_{\text{inv}-o} = \left(1 + s^2 L_1 C + s C G_c G_d - G_f G_d\right) / \Delta \tag{9}$$

$$Y_{\text{pll}} = T_{\text{pll}} G_{\text{plant}}. \tag{10}$$

The inverter output impedance with the PLL effect $(Z_{o-\text{con}})$ can be found by solving the transfer function from u_{pcc} to i_g in Fig. 4, and is given by (11). It is worth noting that $Z_{o-\text{con}}$ bridges i_g and u_{pcc} at the same frequency, and it is thus referred to as the conventional single-frequency output impedance in this article

$$Z_{o-\text{con}} = 1/Y_{o-\text{con}} = -1/\left(T_{\text{pll}} \cdot G_{\text{plant}} - Y_{\text{inv}-o}\right). \tag{11}$$

C. Limitations of $Z_{o-\text{con}}$ in Harmonic Stability Analysis

Based on the ISC, the stability of the grid-tied inverter can be predicted by applying the Nyquist criterion to the impedance ratio $Z_{\text{pcc}}/Z_{o-\text{con}}$. Although the conventional impedance model $Z_{o-\text{con}}$ is simple and effective to some extent, it does have its own limitations, especially when the weak grid is connected. For example, the typical experimental waveform of the FCE under the condition that the PCC voltage is perturbed at the frequency 127 Hz is shown in Fig. 5. It is observed that the grid current is composed by the corresponding component (127 Hz) and the coupling components (27 Hz, 227 Hz). Additional loops caused by the FCE are closed through the grid impedance, which is verified to worsen the three-phase system stability and is not well studied in the single-phase system. The reasons why $Z_{o-\text{con}}$ fails to exactly identify the harmonic stability in Fig. 5, are contributed by the two nonrigorous assumptions made in the derivation of (11).

First, the FCE is overlooked. By combining (3) and (4), $\tilde{\theta}(s)$ can be extracted as

$$\tilde{\theta}(s) = 0.5G_{\text{pll}}(s)\left\{\begin{array}{l} j\left[\tilde{u}_\alpha(s-j\omega_0) - \tilde{u}_\alpha(s+j\omega_0)\right] \\ +\tilde{u}_\beta(s-j\omega_0)+\tilde{u}_\beta(s+j\omega_0)\end{array}\right\}. \tag{12}$$

Shifting (12) in the s-domain and substituting it into (5), the current reference $\tilde{i}_{\text{ref}}(s)$ can be derived as the sum of three parts $\tilde{i}_{\text{ref}-11}(s)$, $\tilde{i}_{\text{ref}-p}(s)$, and $\tilde{i}_{\text{ref}-n}(s)$, which are provided as

$$\tilde{i}_{\text{ref}-11}(s) = 0.25I_m\left\{\begin{array}{l}\left[\tilde{u}_\alpha(s)+j\tilde{u}_\beta(s)\right]G_{\text{pll}}(s-j\omega_0) \\ +\left[\tilde{u}_\alpha(s)-j\tilde{u}_\beta(s)\right]G_{\text{pll}}(s+j\omega_0)\end{array}\right\} \tag{13}$$

$$\tilde{i}_{\text{ref}-p}(s) = 0.25I_m\left[-\tilde{u}_\alpha(s+2j\omega_0)-j\tilde{u}_\beta(s+2j\omega_0)\right] \times G_{\text{pll}}(s+j\omega_0) \tag{14}$$

$$\tilde{i}_{\text{ref}-n}(s) = 0.25I_m\left[-\tilde{u}_\alpha(s-2j\omega_0)-j\tilde{u}_\beta(s-2j\omega_0)\right] \times G_{\text{pll}}(s-j\omega_0) \tag{15}$$

where $\tilde{i}_{\text{ref}-11}(s)$, $\tilde{i}_{\text{ref}-p}(s)$, and $\tilde{i}_{\text{ref}-n}(s)$ denote the current reference corresponding to u_{pcc} in the $\alpha\beta$ frame at the frequency ω, $\omega+2\omega_0$, and $\omega-2\omega_0$, respectively. It is found that $\tilde{i}_{\text{ref}}(s)$ at a given frequency ω is related to u_{pcc} not only at the same frequency ω, but also at the two coupled frequencies $\omega \pm 2\omega_0$, which complies with the FCE phenomenon screened in Fig. 5. The neglect of the FCE described by (14) and (15) poses a challenge to predict the resonances and the stability exactly.

Second, (13) is simplified as (6) under the condition that $\tilde{u}_\alpha = j\tilde{u}_\beta$, which is not always satisfied in the single-phase grid-tied inverter except at certain odd frequencies. Therefore, the impedance $Z_{o-\text{con}}$ is not rigorously derived. It is also worth noting that the PCC voltage on the β-axis $\tilde{u}_\beta$ is always lagging $\tilde{u}_\alpha$ 90° in the three-phase symmetric system. The current $\tilde{i}_{\text{ref}-n}(s)$ shown in (15) is thus omitted, which leads to the FCE that $\tilde{i}_{\text{ref}}(s)$ is coupled with u_{pcc} at the frequency s and $s+2j\omega_0$ in the three-phase system. Therefore, the FCE works quite differently between the single-phase system and the three-phase system.

III. Multifrequency Model of the Grid-Tied Inverter

Since the existed single-frequency impedance model in (11) only reflects the one-to-one frequency mapping from u_{pcc} to i_g, it fails to identify the harmonic stability problem exemplified in Fig. 5. This section introduces the multifrequency principle to model the PLL of the single-phase inverter, and a 3 × 3 MAM is proposed to avoid the ambiguous estimation of the inverter output impedance.

A. Proposed MAM Model

The multifrequency principle is commonly used to account for the coupled harmonics caused by the nonlinear pulsewidth modulator [32], [33]. Applications of the multifrequency principle in the impedance modeling can be found in the model of the three-phase inverter [24] and the modular multilevel converter [34]. As the PLL is also characterized by the nonlinearity inside the Park transformation and the current reference generator, the admittance model of the single-phase inverter can also be developed by migrating the multifrequency principle when the FCE needs to be captured.

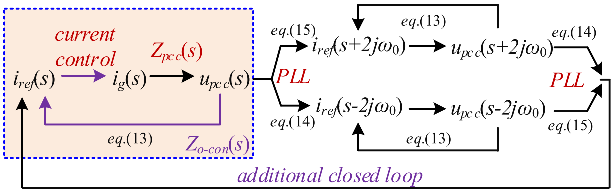

Fig. 6. Signal flow diagram of a single-phase inverter under the weak grid.

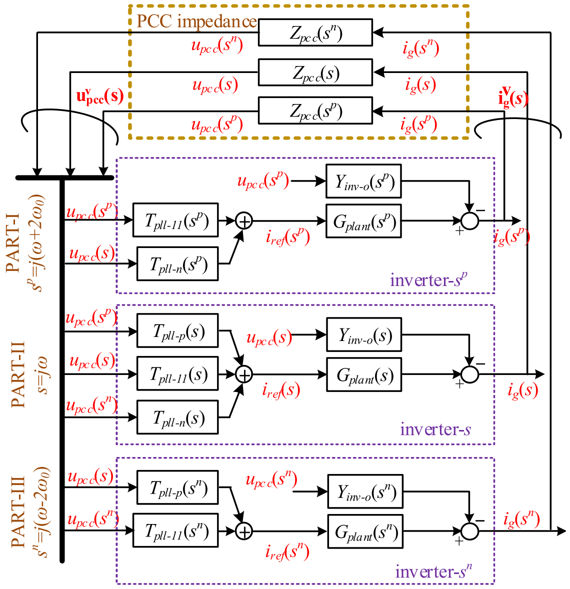

Fig. 7. Multifrequency control diagram of the single-phase inverter.

Fig. 6 shows the signal flow of a single-phase inverter when the FCE is taken into consideration. Specifically, in terms of the grid current i_g at the analyzed frequency ω, it will flow through the PCC impedance $Z_{\text{pcc}}(s)$, and thus generate the voltage at the frequency ω (i.e., $u_{\text{pcc}}(s)$), which forms the conventional closed loop for deriving $Z_{o-\text{con}}(s)$ (the dashed box in Fig. 6). The PCC voltage $u_{\text{pcc}}(s)$ is coupled with the current reference i_{ref} at the frequency $\omega \pm 2\omega_0$ [i.e., $i_{\text{ref}}(s+2j\omega_0)$ and $i_{\text{ref}}(s-2j\omega_0)$] due to the FCE described by (14) and (15). As the grid current i_g tracks the current reference i_{ref} at the coupled frequency $\omega \pm 2\omega_0$ by the current regulator, the induced grid current [i.e., $i_g(s+2j\omega_0)$ and $i_g(s-2j\omega_0)$] together with the PCC impedance will generate the corresponding PCC voltage [i.e., $u_{\text{pcc}}(s+2j\omega_0)$ and $u_{\text{pcc}}(s-2j\omega_0)$], which will couple into the current reference $i_{\text{ref}}(s)$ at the frequency ω. Thus, an additional closed loop is formed in Fig. 6, which may challenge the system stability under the weak grid.

Based on Figs. 4 and 6, the multifrequency control diagram of a single-phase inverter with the additional closed loops is constructed as Fig. 7, wherein the Laplace operator "s" with the superscripts "p" and "n" denote the positively coupled frequency $s+2j\omega_0$ and the negatively coupled frequency $s-2j\omega_0$, respectively. It is noted that the two symbols “p” and “n” just denote the coupled frequencies other than the positive sequence and the negative sequence used in three-phase system.

Before deriving the transfer functions in Fig. 7, $G_{osg\beta}(s)$ is defined as the transfer function from u_{pcc} to u_β, and is given by

$$u_\beta(s) = G_{osg\beta}(s)u_{\text{pcc}}(s). \tag{16}$$

Starting with part-II in Fig. 7, the current reference at the frequency ω is generated by the PCC voltage at the frequency ω, $\omega + 2\omega_0$, and $\omega - 2\omega_0$ based on (13)–(15). $T_{\text{pll}-11}(s)$, $T_{\text{pll}-p}(s)$, and $T_{\text{pll}-n}(s)$ denote the transfer functions from u_{pcc} at ω, $\omega + 2\omega_0$, and $\omega - 2\omega_0$ to i_{ref} at ω [i.e., $u_{\text{pcc}}(s) \to i_g(s)$, $u_{\text{pcc}}(s + 2j\omega_0) \to i_g(s)$, $u_{\text{pcc}}(s - 2j\omega_0) \to i_g(s)$], respectively, and their mathematical expressions are deduced as

$$\begin{aligned} T_{\text{pll}-11}(s) &= I_m H_{\text{pll}-11}(s) \\ &= 0.25 I_m \left(G_{osg\alpha}(s) + jG_{osg\beta}(s)\right) G_{\text{pll}}\left(s - j\omega_0\right) \\ &\quad + 0.25 I_m \left(G_{osg\alpha}(s) - jG_{osg\beta}(s)\right) G_{\text{pll}}\left(s + j\omega_0\right) \end{aligned} \tag{17}$$

$$\begin{aligned} T_{\text{pll}-p}(s) &= I_m H_{\text{pll}-p}(s) \\ &= -0.25 I_m \left[G_{osg\alpha}(s+2j\omega_0) + jG_{osg\beta}(s+2j\omega_0)\right] \\ &\quad \times G_{\text{pll}}\left(s + j\omega_0\right) \end{aligned} \tag{18}$$

$$\begin{aligned} T_{\text{pll}-n}(s) &= I_m H_{\text{pll}-n}(s) \\ &= 0.25 I_m\left[-G_{osg\alpha}(s-2j\omega_0) + jG_{osg\beta}(s-2j\omega_0)\right] \\ &\quad \times G_{\text{pll}}\left(s - j\omega_0\right) \end{aligned} \tag{19}$$

where $H_{\text{pll}-11}(s)$, $H_{\text{pll}-p}(s)$, and $H_{\text{pll}-n}(s)$ are the corresponding transfer functions of $T_{\text{pll}-11}(s)$, $T_{\text{pll}-p}(s)$, and $T_{\text{pll}-n}(s)$ with the current reference I_m extracted. The subscripts “p” and “n” mean that, compared with the frequency of the coupled reference, the frequency of the input voltage u_{pcc} is shifted positively and negatively, respectively.

With respect to part-I and part-III in Fig. 7, $T_{\text{pll}-11}(s^p)$ and $T_{\text{pll}-11}(s^n)$ are the one-to-one frequency mapping in the coupled loops, which can be readily obtained by substituting s^p and s^n into (17). $T_{\text{pll}-p}(s^p)$ and $T_{\text{pll}-n}(s^n)$ denote the transfer functions from u_{pcc} at ω to i_{ref} at $\omega + 2\omega_0$, and $\omega - 2\omega_0$ [i.e., $u_{\text{pcc}}(s) \to i_g(s + 2j\omega_0)$, $u_{\text{pcc}}(s) \to i_g(s - 2j\omega_0)$], respectively.

According to Fig. 7, the single-phase inverter-grid system can be seen as a multi-input multi-output system where the input 3 × 1 vector $\mathbf{u}^{\text{v}}_{\text{pcc}}(\mathbf{s})$ is composed of $u_{\text{pcc}}(s^p)$, $u_{\text{pcc}}(s)$, and $u_{\text{pcc}}(s^n)$, and the output 3 × 1 vector $\mathbf{i}^{\text{v}}_{\mathbf{g}}(\mathbf{s})$ is made up of $i_g(s^p)$, $i_g(s)$, and $i_g(s^n)$. Therefore, the current reference i_{ref} at the three coupled frequencies corresponding to $\mathbf{u}^{\text{v}}_{\text{pcc}}(\mathbf{s})$ can be derived as

$$\begin{aligned} \begin{bmatrix} i_{\text{ref}}(s^p) \\ i_{\text{ref}}(s) \\ i_{\text{ref}}(s^n) \end{bmatrix} &= \overbrace{\begin{bmatrix} T_{\text{pll}-11}(s^p) & T_{\text{pll}-n}(s^p) & 0 \\ T_{\text{pll}-p}(s) & T_{\text{pll}-11}(s) & T_{\text{pll}-n}(s) \\ 0 & T_{\text{pll}-p}(s^n) & T_{\text{pll}-11}(s^n) \end{bmatrix}}^{T_{\text{pll}}(s)} \begin{bmatrix} u_{\text{pcc}}\left(s^p\right) \\ u_{\text{pcc}}\left(s\right) \\ u_{\text{pcc}}\left(s^n\right) \end{bmatrix} \\ &= I_m \overbrace{\begin{bmatrix} H_{\text{pll}-11}(s^p) & H_{\text{pll}-n}(s^p) & 0 \\ H_{\text{pll}-p}(s) & H_{\text{pll}-11}(s) & H_{\text{pll}-n}(s) \\ 0 & H_{\text{pll}-p}(s^n) & H_{\text{pll}-11}(s^n) \end{bmatrix}}^{H_{\text{PLL}}(s)} \\ &\quad \times \begin{bmatrix} u_{\text{pcc}}\left(s^p\right) \\ u_{\text{pcc}}\left(s\right) \\ u_{\text{pcc}}\left(s^n\right) \end{bmatrix} \end{aligned} \tag{20}$$

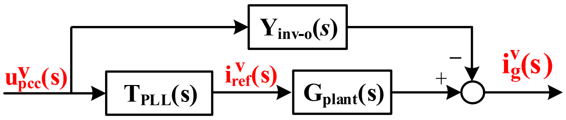

Fig. 8. Compact form of the multifrequency control diagram.

where $\mathbf{H_{PLL}}(\mathbf{s})$ is the transfer function matrix with I_m extracted from $\mathbf{T_{PLL}}(\mathbf{s})$.

According to (20), the grid current i_g at the three coupled frequencies can be deduced as

$$\mathbf{i}^{\text{v}}_{\mathbf{g}}\left(\mathbf{s}\right) = \mathbf{Y}_{3\times 3}\left(\mathbf{s}\right) \cdot \mathbf{u}^{\text{v}}_{\mathbf{pcc}}\left(\mathbf{s}\right) \tag{21}$$

where $\mathbf{Y_{3\times 3}}(\mathbf{s})$ is the proposed 3 × 3 MAM model, and is expressed by

$$\begin{aligned} \mathbf{Y_{3\times 3}}(s) &= \overbrace{\mathbf{G_{plant}}(\mathbf{s}) \cdot \mathbf{T_{PLL}}(\mathbf{s})}^{\mathbf{Y_{inv-PLL}}(s)} + \mathbf{Y_{inv-o}}(\mathbf{s}) \\ &= I_m \cdot \overbrace{\mathbf{G_{plant}}(\mathbf{s}) \cdot \mathbf{H_{PLL}}(\mathbf{s})}^{\mathbf{H_{inv-PLL}}(s)} + \mathbf{Y_{inv-o}}(\mathbf{s}) \end{aligned} \tag{22}$$

where $\mathbf{G_{plant}}(\mathbf{s})$ is the 3 × 3 diagonal matrix $[G_{\text{plant}}(s^p)\,0\,0;\,0\,G_{\text{plant}}(s)\,0;\,0\,0\,G_{\text{plant}}(s^n)]$, and $\mathbf{Y_{inv-o}}(\mathbf{s})$ is the 3 × 3 diagonal matrix $[Y_{\text{inv}-o}(s^p)\,0\,0;\,0\,Y_{\text{inv}-o}(s)\,0;\,0\,0\,Y_{\text{inv}-o}(s^n)]$.

It can be found that the FCE of PLL is included in $\mathbf{T_{PLL}}(\mathbf{s})$ (off-diagonal matrix), which adds another admittance $\mathbf{Y_{inv-PLL}}(\mathbf{s})$ in parallel with the original admittance matrix $\mathbf{Y_{inv-o}}(\mathbf{s})$, and consequently shapes the output admittance.

According to (22) and Fig. 7, the multifrequency control diagram is further shown in Fig. 8 with a more compact form, where the transfer functions and the signals are replaced by the corresponding 3 × 3 matrix and 3 × 1 vector, respectively. Different from the existed impedance model of the single-phase grid-connected inverter, the off-diagonal 3 × 3 matrix $\mathbf{T_{PLL}}(\mathbf{s})$ is used to capture the FCE of the PLL. It is also worth noting that the dimension of $\mathbf{Y_{3\times 3}}(\mathbf{s})$ is different from that of the three-phase inverter, wherein the current of the three-phase inverter is controlled in $\alpha\beta$ frame or dq frame, resulting in 2 × 2 impedance matrix. However, in single-phase grid-connected inverter, the current is controlled on only one α-axis whereas the frequency components of the current are decomposed based on the multifrequency principle, resulting in 3 × 3 matrix.

B. Stability Prediction Based on the GNC

As the admittance matrix $\mathbf{Y_{3\times 3}}$ is characterized by the asymmetric behavior, the GNC should be used to evaluate the inverter-grid system stability [35], [36].

When the inverter is connected to the grid with the PCC impedance Z_{pcc}, the voltage at the PCC satisfies

$$\mathbf{u}_{\mathbf{pcc}}^{\mathbf{v}}(\mathbf{s}) = \mathbf{Z}_{\mathbf{pcc}}(\mathbf{s}) \cdot \mathbf{i}_{\mathbf{g}}^{\mathbf{v}}(\mathbf{s}) + \mathbf{u}_{\mathbf{g}}^{\mathbf{v}}(\mathbf{s}) \tag{23}$$

where $\mathbf{Z}_{\text{pcc}}(\mathbf{s})$ is the 3×3 diagonal matrix of the grid impedance, i.e., $[\mathrm{Z}_{\text{pcc}}(s^p)\,0\,0;\ 0\,\mathrm{Z}_{\text{pcc}}(\mathrm{s})\,0;\ 0\,0\,\mathrm{Z}_{\text{pcc}}(s^n)]$. Substituting (23) into (21), the characteristic equation is derived as

$$[\mathbf{I} - \mathbf{Y}_{3\times 3}(\mathbf{s}) \cdot \mathbf{Z}_{\mathbf{pcc}}(\mathbf{s})]\, \mathbf{i}_{\mathbf{g}}^{\mathbf{v}}(\mathbf{s}) = \mathbf{Y}_{3\times 3}(\mathbf{s}) \cdot \mathbf{u}_{\mathbf{g}}^{\mathbf{v}}(\mathbf{s}) \tag{24}$$

where $\mathbf{I}$ is a 3×3 unit matrix, the impedance ratio $\Re$ is given by

$$\Re(\mathbf{s}) = \mathbf{Y}_{3\times 3}(\mathbf{s}) \cdot \mathbf{Z}_{\mathbf{pcc}}(\mathbf{s}). \tag{25}$$

The inverter-grid system stability can be predicted by checking the Nyquist plot of the determinant $\mathbf{I} - \mathbf{Y}_{\mathbf{3\times 3}}(\mathbf{s}) \cdot \mathbf{Z}_{\text{pcc}}(\mathbf{s})$ in terms of the critical point (0, j0) [36], or by checking the frequency responses of the eigenvalues of the impedance ratio $\Re(s)$ in terms of $(-1, \text{j}0)$. The latter conventional method is adopted in this article, and the eigenvalues are calculated with the aid of the computational software, which are given by

$$\det\left[\lambda \mathbf{I} - \mathbf{Y}_{3\times 3}(\mathbf{s}) \cdot \mathbf{Z}_{\mathbf{pcc}}(\mathbf{s})\right] = 0. \tag{26}$$

IV. DEVELOPED SINGLE-FREQUENCY IMPEDANCE MODEL

Although the MAM model is effective in evaluating the influence of the PLL on the inverter-grid system stability, it is not intuitive to identify where the harmonic resonances are possibly triggered, and it is also hard to experimentally measure the couplings. To facilitate the resonant frequency analysis as the conventional output impedance model does, it is required to have knowledge of the single-frequency output impedance with the embedded multifrequency principle. Therefore, a developed single-frequency output impedance model is elaborated in this section.

A. Derivation of the Developed Inverter Output Impedance

Since the single-frequency impedance model is derived from a single-input single-output system, the relationships among the elements of the input vector $\mathbf{u}_{\text{pcc}}^{\text{v}}(\mathbf{s})$ in Fig. 8 need to be figured out. By substituting (21) into (23), it is derived that

$$[\mathbf{I} - \mathbf{Z}_{\mathbf{pcc}}(\mathbf{s}) \cdot \mathbf{Y}_{3\times 3}(\mathbf{s})] \cdot \mathbf{u}_{\mathbf{pcc}}^{\mathbf{v}}(\mathbf{s}) - \mathbf{u}_{\mathbf{g}}^{\mathbf{v}}(\mathbf{s}) = \mathbf{0}. \tag{27}$$

The closed-loop transfer functions from the PCC voltage u_{pcc} at the analyzed frequency ω to u_{pcc} at the two coupled frequencies (i.e., $u_{\text{pcc}}(s) \rightarrow u_{\text{pcc}}(s + 2j\omega_0)$ and $u_{\text{pcc}}(s) \rightarrow u_{\text{pcc}}(s - 2j\omega_0)$) can be derived from (27) and defined as $G_p(s)$ and $G_n(s)$, respectively, which are provided as

$$G_p = \frac{I_m Z_{\text{pcc}}(s^p) G_{\text{plant}}(s^p) H_{\text{pll}-n}(s^p)}{1 - Z_{\text{pcc}}(s^p)\left[I_m G_{\text{plant}}(s^p) H_{\text{pll}-11}(s^p) + Y_{\text{inv}-o}(s^p)\right]} \tag{28}$$

$$G_n = \frac{I_m Z_{\text{pcc}}(s^n) G_{\text{plant}}(s^n) \cdot H_{\text{pll}-p}(s^n)}{1 - Z_{\text{pcc}}(s^n)\left[I_m G_{\text{plant}}(s^n) H_{\text{pll}-11}(s^n) + Y_{\text{inv}-o}(s^n)\right]}. \tag{29}$$

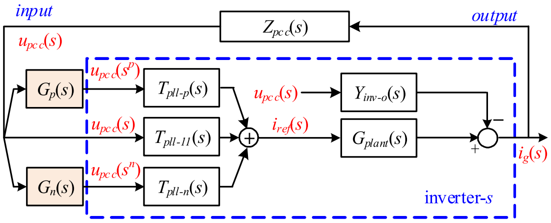

Fig. 9. Control diagram with the embedded multifrequency principle.

Therefore, the single-frequency control diagram at the analyzed frequency ω is constructed as Fig. 9. The transfer function from $u_{\text{pcc}}(s)$ to the current $i_g(s)$ can be easily deduced as (30), and it is defined as $Y_{op}|_{(Z\text{pcc},\, Im)}$

$$\begin{aligned} Y_{op}|_{(Z_{\text{pcc}}, I_m)} = \frac{1}{Z_{op}|_{(Z_{\text{pcc}}, I_m)}} &= \overbrace{\underbrace{I_m H_{\text{pll}-11} G_{\text{plant}}}_{Y_{11}} + Y_{\text{inv}-o}}^{Y_{o-\text{con}}} \\ &\quad + \underbrace{I_m G_p H_{\text{pll}-p} G_{\text{plant}}}_{Y_p|_{(Z_{\text{pcc}}, I_m)}} + \underbrace{I_m G_n H_{\text{pll}-n} G_{\text{plant}}}_{Y_n|_{(Z_{\text{pcc}}, I_m)}} \end{aligned} \tag{30}$$

where $Z_{op}|_{(Z\text{pcc},\, Im)}$ is the developed single-frequency output impedance with the embedded multifrequency principle at a certain PCC impedance Z_{pcc}. $Y_p|_{(Z\text{pcc},\, Im)}$ and $Y_n|_{(Z\text{pcc},\, Im)}$ are the positively coupled and the negatively coupled equivalent admittance at a certain $(Z_{\text{pcc}},\ I_m)$, respectively. $Y_{o-\text{con}}$ is the conventional admittance, which is composed of the equivalent admittance of the one-to-one frequency mapping Y_{11} and the output admittance without the PLL effect $Y_{\text{inv}-o}$.

It is emphasized that the impedance seen from the PCC Z_{pcc} appears in the proposed impedance $Z_{op}|_{(Z\text{pcc},\, Im)}$, which means that the inverter output impedance depends not only on the parameters of the inverter itself, but also on the PCC impedance. This phenomenon appears when the analyzed system is characterized by the FCE or the mirror frequency effect. Although it is counter intuitive, it will be further experimentally validated to have a nonnegligible impact on the inverter-grid system stability.

B. Stability Analysis Based on the Nyquist Criterion

The ISC is widely used to analyze the behavior of the interconnected load-source system [25], which is commonly conducted by applying the Nyquist stability criterion to the impedance ratio of the inverter output impedance to the PCC impedance. Based on (30) and the conventional impedance model in [27] and [28], the developed single-frequency impedance model of the inverter-grid system can be readily established as Fig. 10, which intuitively illustrates how the FCE affects the system stability.

From Fig. 10, it is observed that two additional admittance $Y_p|_{(Z\text{pcc},\, Im)}$ and $Y_n|_{(Z\text{pcc},\, Im)}$ related with Z_{pcc} are formed in parallel with the conventional admittance $Y_{o-\text{con}}$, which means that the inverter output impedance is reshaped when the FCE of PLL is taken into consideration. Similar to [26], the stability can be identified by checking whether the impedance

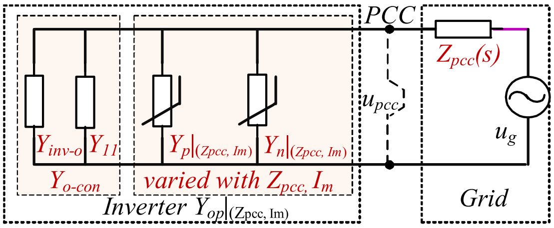

Fig. 10. Developed single-frequency impedance model of the single-phase inverter-grid system.

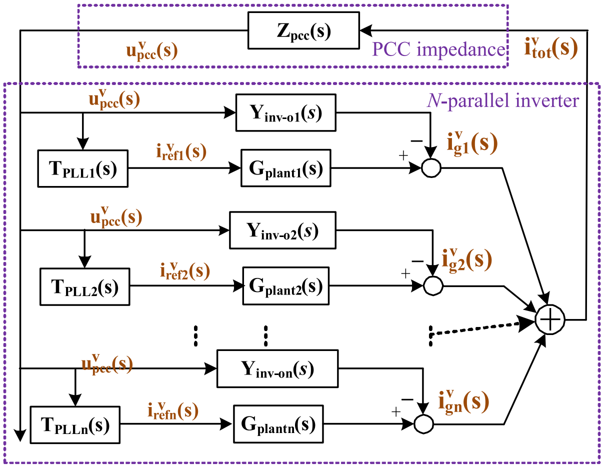

Fig. 11. Multifrequency control diagram of *n*-parallel inverter system.

ratio $Z_{\text{pcc}}/\,Z_{op}|_{(Z\text{pcc},\,Im)}$ satisfies the Nyquist stability criterion. The harmonic performance can be predicted by finding the PM corresponding to the intersected frequency of the two magnitude-frequency curves $Z_{op}|_{(Z\text{pcc},\,Im)}$ and Z_{pcc}. If the PM is not large enough, e.g., smaller than 45°, the harmonics at the intersected frequency of $Z_{op}|_{(Z\text{pcc},\,Im)}$ and Z_{pcc} are possibly excited. If the PM is sufficient, the system stability is ensured with the outcome of a better current quality. The only difference from [26] is that $Z_{op}|_{(Z\text{pcc},\,Im)}$ should be repeatedly calculated under different Z_{pcc}, since the output impedance varies along with Z_{pcc}.

V. IMPEDANCE MODEL OF *N*-PARALLEL INVERTER SYSTEM

The proposed impedance modeling method is extended into the *n*-parallel inverter system to illustrate how the FCE affects the output impedance characteristic of the *n*-parallel system.

A. Impedance Modeling

According to Fig. 8, the multifrequency control diagram for the *n*-parallel inverter system is constructed as Fig. 11, wherein the subscripts $1, 2, \ldots, n$ denote the numeric identifier of the inverter, and the 3 × 1 vector $\mathbf{i}^{\text{v}}_{\mathbf{tot}}(\text{s})$ (i.e., $i_{\text{tot}}(s^p)$, $i_{\text{tot}}(s)$, and $i_{\text{tot}}(s^n)$) means the total grid current of the *n*-parallel system.

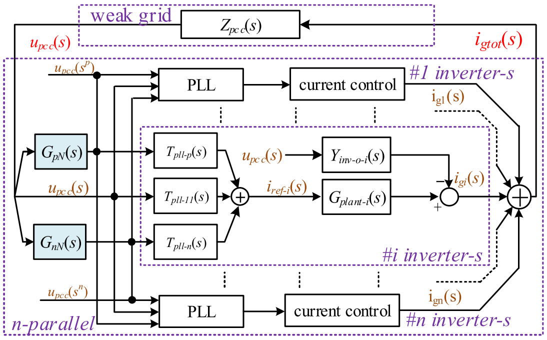

Fig. 12. Single-frequency control diagram of *n*-parallel inverter system.

Based on (21), $\mathbf{i}^{\text{v}}_{\mathbf{tot}}(\text{s})$ is easily deduced as

$$\mathbf{i}^{\mathbf{v}}_{\mathbf{tot}}(\mathbf{s}) = \sum_{i=1,2\ldots}^{n} \mathbf{i}^{\mathbf{v}}_{\mathbf{gi}}(\mathbf{s}) = \sum_{i=1,2\ldots}^{n} \mathbf{Y}_{3\times3-i}(\mathbf{s}) \cdot \mathbf{u}^{\mathbf{v}}_{\mathbf{pcc}}(\mathbf{s}) \quad (31)$$

wherein the subscript *i* symbolizes the #*i* inverter.

The PCC voltage $\mathbf{u}^{\text{v}}_{\text{pcc}}(\text{s})$ shown in (23) is modified as

$$\mathbf{u}^{\mathbf{v}}_{\mathbf{pcc}}(\mathbf{s}) = \mathbf{Z}_{\mathbf{pcc}}(\mathbf{s}) \cdot \mathbf{i}^{\mathbf{v}}_{\mathbf{tot}}(\mathbf{s}) + \mathbf{u}^{\mathbf{v}}_{\mathbf{g}}(\mathbf{s}). \quad (32)$$

By substituting (31) into (32), the relationships among the elements of the input vector $\mathbf{u}^{\text{v}}_{\text{pcc}}(\text{s})$ is derived as

$$\left[\mathbf{I} - \mathbf{Z}_{\mathbf{pcc}}(\mathbf{s}) \cdot \sum_{i=1,2\ldots}^{n} \mathbf{Y}_{3\times3-i}(\mathbf{s})\right] \cdot \mathbf{u}^{\mathbf{v}}_{\mathbf{pcc}}(\mathbf{s}) - \mathbf{u}^{\mathbf{v}}_{\mathbf{g}}(\mathbf{s}) = \mathbf{0}. \quad (33)$$

Based on (33), the closed-loop transfer functions from the PCC voltage u_{pcc} at the analyzed frequency ω to u_{pcc} at the two coupled frequencies [i.e., $u_{\text{pcc}}(s) \rightarrow u_{\text{pcc}}(s + 2j\omega_0)$ and $u_{\text{pcc}}(s) \rightarrow u_{\text{pcc}}(s - 2j\omega_0)$] can be derived and defined as the coupled transfer functions G_{pN} and G_{nN}, respectively, which are provided as

$$G_{pN} = \frac{Z_{\text{pcc}}(s^p) \sum\limits_{i=1,\ldots}^{n} I_{mi} G_{\text{plant}-i}(s^p) \cdot H_{\text{pll}-n-i}(s^p)}{1 - Z_{\text{pcc}}(s^p) \sum\limits_{i=1,2,..}^{n} [I_{mi} G_{\text{plant}-i}(s^p) H_{\text{pll}-11-i}(s^p) + Y_{\text{inv}-o-i}(s^p)]} \quad (34)$$

$$G_{nN} = \frac{Z_{\text{pcc}}(s^n) \sum\limits_{i=1,\ldots}^{n} I_{mi} G_{\text{plant}-i}(s^n) \cdot H_{\text{pll}-p-i}(s^n)}{1 - Z_{\text{pcc}}(s^n) \sum\limits_{i=1,2,\ldots}^{n} [I_{mi} G_{\text{plant}-i}(s^n) H_{\text{pll}-11-i}(s^n) + Y_{\text{inv}-o-i}(s^n)]} \quad (35)$$

where it is found G_{pN} and G_{nN} are related to the PCC impedance and the parameters of every inverter in the parallel system.

According to (34), (35), and Fig. 11, the single-frequency control diagram of the *n*-parallel system at the analyzed frequency ω is established as Fig. 12, which describes the one-to-one frequency mapping from u_{pcc} to the total current i_{tot}. The output impedance of the parallel system is defined as $Z_{oN}|_{Z\text{pcc}}$, which is obtained by solving the the transfer function from $u_{\text{pcc}}(s)$ to $i_{\text{tot}}(s)$ in Fig. 12 and is shown as

$$Y_{oN}|_{Z_{\text{pcc}}} = \frac{1}{Z_{oN}|_{Z_{\text{pcc}}}} = \sum_{i=1,2\ldots}^{n} \underbrace{I_{mi}G_{pN}H_{\text{pll}-p-i}G_{\text{plant}-i}}_{Y_{p-i}(s)|_{Z_{\text{pcc}}}} + \sum_{i=1,2\ldots}^{n}\left[\overbrace{I_{mi}G_{nN}H_{\text{pll}-n-i}G_{\text{plant}-i}}^{Y_{n-i}(s)|_{Z_{\text{pcc}}}} + \overbrace{\underbrace{I_{mi}H_{\text{pll}-11-i}G_{\text{plant}-i}}_{Y_{11-i}(s)} + Y_{\text{inv}-o-i}}^{Y_{o\text{-con}-i}(s)}\right]. \tag{36}$$

Therefore, the output impedance $Z_{oN}|_{Z\text{pcc}}$ of the n-parallel system depends not only on the parameters of all the inverters, but also on the PCC impedance. The harmonic stability of the parallel system is assessed by applying the ISC to $Z_{oN}|_{Z\text{pcc}}/Z_{\text{pcc}}$.

B. Analysis of the n-Parallel Homogeneous-Inverter System

As often the case, the inverters installed at the PCC are commonly manufactured by the same firm, and have the same type, which means that it is reasonable to assume all inverters to be equal. In this case, i.e., the n-parallel homogeneous-inverter system, the output impedance of the parallel system is defined as $Z_{oHN}|_{(Z\text{pcc},\,\text{Imtot})}$, which is simplified from (36) and provided as

$$\begin{aligned} Y_{oHN}|_{(Z_{\text{pcc}},I_{m\text{tot}})} &= \frac{1}{Z_{oHN}|_{(Z_{\text{pcc}},I_{m\text{tot}})}} \\ &= \underbrace{nY_{\text{inv}-o} + H_{\text{pll}-11}G_{\text{plant}}I_{m\text{tot}}}_{Y_{oN-\text{con}}} \\ &\quad + \underbrace{G_{pN}H_{\text{pll}-p}G_{\text{plant}}I_{m\text{tot}}}_{Y_{pN}|_{(Z_{\text{pcc}},I_{m\text{tot}})}} \\ &\quad + \underbrace{G_{nN}H_{\text{pll}-n}G_{\text{plant}}I_{m\text{tot}}}_{Y_{nN}|_{(Z_{\text{pcc}},I_{m\text{tot}})}} \end{aligned} \tag{37}$$

where $I_{m\text{tot}}$ is the amplitude of the total grid current i_{tot}, $Y_{oN-\text{con}}$ is the conventional output admittance without the influence of Z_{pcc}. $Y_{pN}|_{(Z\text{pcc},\,\text{Imtot})}$, $Y_{nN}|_{(Z\text{pcc},\,\text{Imtot})}$ are the positively coupled and the negatively coupled equivalent admittance at a certain $(Z_{\text{pcc}},\ I_{m\text{tot}})$. The coupled transfer functions G_{pN} and G_{nN} are derived from (34) and (35), and are expressed by

$$G_{pN} = \frac{nZ_{\text{pcc}}(s^p)G_{\text{plant}}(s^p)\cdot H_{\text{pll}-n}(s^p)\frac{1}{n}\sum\limits_{i=1,2\ldots}^{n} I_{mi}}{1-nZ_{\text{pcc}}(s^p)\left[Y_{\text{inv}-o}(s^p)+G_{\text{plant}}(s^p)H_{\text{pll}-11}(s^p)\frac{1}{n}\sum\limits_{i=1,2\ldots}^{n} I_{mi}\right]} \tag{38}$$

$$G_{nN} = \frac{nZ_{\text{pcc}}(s^n)G_{\text{plant}}(s^n)\cdot H_{\text{pll}-p}(s^n)\frac{1}{n}\sum\limits_{i=1,2\ldots}^{n} I_{mi}}{1-nZ_{\text{pcc}}(s^n)\left[Y_{\text{inv}-o}(s^n)+G_{\text{plant}}(s^n)H_{\text{pll}-11}(s^n)\frac{1}{n}\sum\limits_{i=1,2\ldots}^{n} I_{mi}\right]}. \tag{39}$$

Equivalent transforms are made in (37) for simplifying the stability analysis through $Z_{oHN}|_{(Z\text{pcc},\,\text{Imtot})}/Z_{\text{pcc}}$. By substituting $I_{m\text{tot}}$ with $n{\cdot}I_{\text{avg}}$ (I_{avg} is the average value), it is obtained that

$$\begin{aligned} &Y_{oHN}|_{(Z_{\text{pcc}},I_{m\text{tot}})} \\ &\quad = n(Y_{\text{inv}-o} + H_{\text{pll}-11}G_{\text{plant}}I_{\text{avg}} + G_{pN}H_{\text{pll}-p}G_{\text{plant}}I_{\text{avg}} \\ &\qquad + G_{nN}H_{\text{pll}-n}G_{\text{plant}}I_{\text{avg}}) \end{aligned} \tag{40}$$

where it is found that the output impedance of the n-parallel system is 1/n times of that of a special inverter with the current I_{avg}. However, it is stressed that the output impedance of this special inverter should be calculated under n times PCC impedance, i.e., $Z_{op}|_{(n\cdot Z\text{pcc},I\text{avg})}$, since the influence of Z_{pcc} on the two transfer functions G_{pN} and G_{nN} is n times larger [see (38) and (39)]. Therefore, if the n-parallel homogeneous inverter is connected to the grid with Z_{pcc}, the output impedance of the parallel system satisfies

$$Z_{oHN}|_{(Z_{\text{pcc}},I_{m\text{tot}})} = (1/n)Z_{op}|_{(n\cdot Z_{\text{pcc}},I_m=I_{\text{avg}})}. \tag{41}$$

Based on (41), two applicable conclusions are made.

1) The stability can be identified by applying the ISC to the impedance ratio $\frac{1}{n}\ Z_{op}|_{(n\cdot Z\text{pcc},\ I\text{avg})}/Z_{\text{pcc}}$, which is equivalent to $Z_{op}|_{(n\cdot Z\text{pcc},I\text{avg})}/n\cdot Z_{\text{pcc}}$. This special impedance ratio is defined as the equivalent system G_{eq}. In other words, the recognition that the PCC impedance is n times amplified in the parallel system is satisfied only for one special inverter with the current I_{avg}.
2) The output impedances of two n-parallel homogeneous-inverter systems are identical if the number n and the total grid current i_{tot} are the same.

VI. CASE STUDY OF SINGLE-PHASE GRID-TIED INVERTERS

Since the experimental measurement of the inverter output impedance is much smoother when the injected power is low (to avoid the overload operation of the Venable instrument power amplifier), and the output impedance keeps invariant for the scaled-down system [27], all the theoretical analyses and the experiments are performed on a scaled-down single-phase

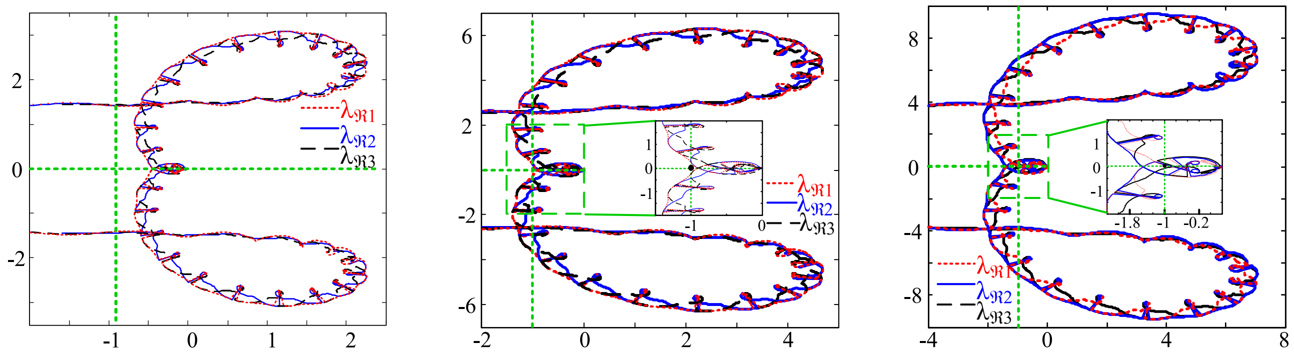

(a) (b) (c)

Fig. 13. Nyquist diagrams of the eigenvalues of $\Re$ under different Z_{pcc}. (a) Case a1: $Z_{\text{pcc}} = s \cdot 1.95\,\text{mH} + 0.4\,\Omega$ (SCR $= 6.66$). (b) Case a2: $Z_{\text{pcc}} = s \cdot 3.85\,\text{mH} + 0.4\,\Omega$ (SCR $= 3.82$). (c) Case a3: $Z_{\text{pcc}} = s \cdot 5.85\,\text{mH} + 0.4\,\Omega$ (SCR $= 2.61$).

TABLE I
PARAMETERS OF THE SCALED-DOWN SINGLE-PHASE INVERTERS

Symbol	Value	Definition
U_n	55 V	nominal grid voltage
I_n	11.3 A	nominal grid current
f_s	15 kHz	control frequency
L_1/R_1	0.75 mH/0.4 Ω	inductance/parasitic resistance
L_2/R_2	0.45 mH/0.25 Ω	inductance/parasitic resistance
C	6.8 μF	filter capacitor
ξ	0.707	damping ratio of the PLL loop
Z_g	0.62 mH+0.4 Ω	grid impedance
Z_{pcc}	1.95 mH+0.4 Ω(6.66), 3.85 mH+0.4 Ω(3.82), 5.85 mH+0.4 Ω(2.61)	PCC equivalent impedance (SCR)
I_m	8 A(0.5), 12 A(0.75), 16 A(1)	amplitude of the current reference
f_b	100 Hz, 220 Hz, 380 Hz	bandwidth of the PLL
G_c	9+15000/s	PI regulator
G_f	0	coefficient of feedforward

inverter, whose parameters are provided in Table I. Moreover, to make a fair comparison with the existed impedance model in [27] and [28], the T/4-delay based PLL is also adopted in this article, which can be described by

$$G_{\text{OSG}-\alpha}(s) = 1, \quad G_{\text{OSG}-\beta}(s) = e^{-T_0 s/4}. \qquad (42)$$

A. *Influence of Z_{pcc} on the Inverter-Grid System Stability*

First, the stability of the single-phase grid-tied inverter under various PCC impedance Z_{pcc} is analyzed by applying the GNC to the proposed 3×3 admittance matrix $\mathbf{Y}_{\mathbf{3\times3}}$. The inverter-grid system parameters are listed in Table I, where I_m and f_b are set as 12 A (0.75 p.u.) and 220 Hz (based on the damping ratio of the PLL loop [28]), respectively. Fig. 13(a)–(c) shows the Nyquist diagrams of the three eigenvalues of the impedance ratio $\Re$ in (26) when L_{pcc} is configured as 1.95, 3.85, and 5.85 mH, respectively. It can be found the scales of the axes are different in Fig. 13(a)–(c), and the stability performance degrades with the increasing Z_{pcc}. Specifically, the inverter works stably with the case a1 and the case a2, but more harmonics are produced with the case a2, and finally it turns unstable with the case a3.

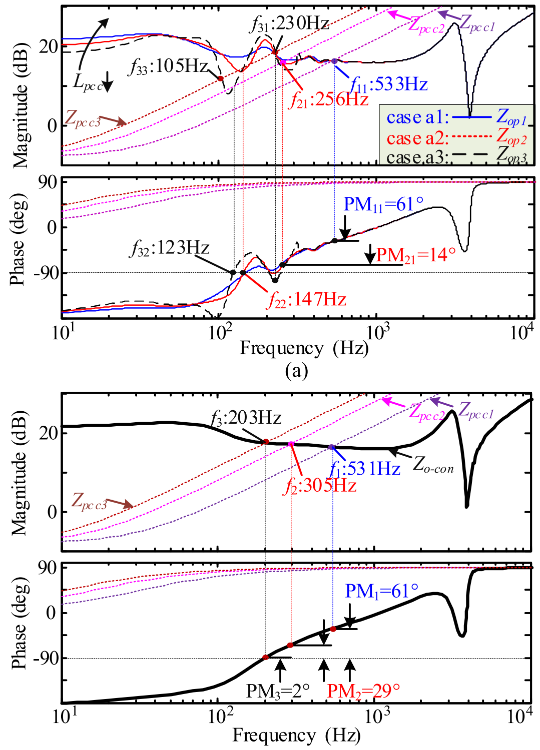

(a)

(b)

Fig. 14. Bode of $Z_{op}|_{Z\text{pcc}}$ and $Z_{o-\text{con}}$ with different Z_{pcc}. ($f_b = 220$ Hz, $I_m = 12$ A). (a) Bode of $Z_{op}|_{(Z\text{pcc},\, Im)}$ under different Z_{pcc}. (b) Bode of $Z_{o-\text{con}}$ under different Z_{pcc}.

It is found that the harmonic frequencies are not intuitively to be predicted according to the three Nyquist diagrams.

To identify where the harmonic frequencies are located, the characteristics of the proposed output impedance $Z_{op}|_{(Z\text{pcc},\, Im)}$ under different Z_{pcc} are studied. Fig. 14(a) and (b) shows the bode diagrams of $Z_{op}|_{(Z\text{pcc},\, Im)}$ corresponding to the three cases in Fig. 13(a)–(c). The bode diagrams of the conventional output impedance $Z_{o-\text{con}}(s)$ are plotted in Fig. 14(b) to make a comparison. Based on the ISC, the stability identified by $Z_{op}|_{(Z\text{pcc},\, Im)}$ is identical to those identified by Fig. 13(a)–(c). Specifically,

TABLE II
PERFORMANCE COMPARISONS UNDER DIFFERENT Z_{PCC}

model	items	case a1 L_{pcc1}=1.95 mH	case a2 L_{pcc2}=3.85 mH	case a3 L_{pcc3}=5.85 mH
$\Re$	stable	yes	yes	no
Z_{op} Fig. 14(a)	line style	Z_{op1}	Z_{op2}	Z_{op3}
	stable	yes	yes	no
	intersected frequency	f_{11}: 533 Hz	f_{21}: 256 Hz f_{22}: 147 Hz	f_{31}: 230 Hz f_{32}: 123 Hz
	phase margin	PM_{11}: 61°	PM_{21}: 14°	
$Z_{o\text{-}con}$ Fig. 14(b)	stable	yes	yes	yes
	intersected frequency	f_1: 531 Hz	f_2: 305 Hz	f_3:203 Hz
	phase margin	PM_1: 63°	PM_2: 29°	PM_3: 3.5°

with respect to the case a1, enough PM ($\mathrm{PM}_{11} = 61°$) is observed at the intersected frequency f_{11} (533 Hz) of the two magnitude-frequency curves Z_{op1} and Z_{pcc}, which means that the inverter-grid system stability is good and the grid current is not prone to be excited at f_{11}. In terms of the case a2, limited PM and GM are found around 256 and 147 Hz in Fig. 14(a), which is different from the frequency 305 Hz predicted by $Z_{o-\mathrm{con}}$ in Fig. 14(b). Therefore, the harmonic frequency of the grid current is predicted to be different by Z_{op2} and $Z_{o-\mathrm{con}}$. In case a3, conflicting stability conclusions are made. It is predicted to be unstable by Z_{op3} when L_{pcc} is 5.85 mH (SCR = 2.61), whereas it is deemed to be stable by $Z_{o-\mathrm{con}}$. The harmonic and stability identified by different models are summarized in Table II.

B. Influence of the Current Reference and the PLL Bandwidth

As the current reference I_m appears in the transfer functions of PLL, e.g., $T_{\mathrm{pll}-11}(s)$, the influence of I_m on the system stability also needs to be identified. With the PCC inductor set as 3.85 mH (SCR = 3.82) and the PLL bandwidth set as 220 Hz, Fig. 15(a) and (b) shows the bode diagrams of the proposed impedance $Z_{op}|_{(Z\mathrm{pcc},\, Im)}$ and the conventional output impedance $Z_{o-\mathrm{con}}$ with I_m varying from 8 A (0.5 p.u.) to 16 A (1 p.u.), respectively.

From Fig. 15, both impedance models indicate that the inverter-grid system stability degrades gradually with the increasing I_m. However, the output impedance profiles of the same I_m are quite different between $Z_{op}|_{(Z\mathrm{pcc},\, Im)}$ and Z_{pcc}. Specifically, in the case b3 ($I_m = 16$ A, 1 p.u.), it is to note that the PM is larger than 0 ($\mathrm{PM}_3 = 15°$) around the intersected frequency 263 Hz of the magnitude-frequency curves $Z_{o-\mathrm{con}3}$ and Z_{pcc} in Fig. 15(b), whereas the PM is negative at the intersected frequency f_{31} and f_{32} of Z_{op3} and Z_{pcc} in Fig. 15(a), which means that conflicting stability predictions are made.

Fig. 16(a) and (b) shows the bode diagrams of $Z_{op}|_{(Z\mathrm{pcc},\, Im)}$ and $Z_{o-\mathrm{con}}$ with the PLL bandwidth f_b increased from 100 to 380 Hz, which is used to reveal the influence of f_b on the inverter-grid system stability. From Fig. 16, it is observed that both impedance models indicate that the system stability degrades with the increasing f_b. It is found that the stability conclusions made by $Z_{o-\mathrm{con}}$ and $Z_{op}|_{(Z\mathrm{pcc},\, Im)}$ are similar when f_b is low. However, inconsistent stability predictions are made when f_b is 380 Hz (case c3), since the PM is larger than 0 ($\mathrm{PM}_3 = 11°$) around the intersected frequency 279 Hz of the magnitude-frequency curves $Z_{o-\mathrm{con}3}$ and Z_{pcc} in Fig. 16(b), and the PM is negative at the intersected frequency f_{31} and f_{32} of the magnitude-frequency curves Z_{op3} and Z_{pcc} in Fig. 16(a).

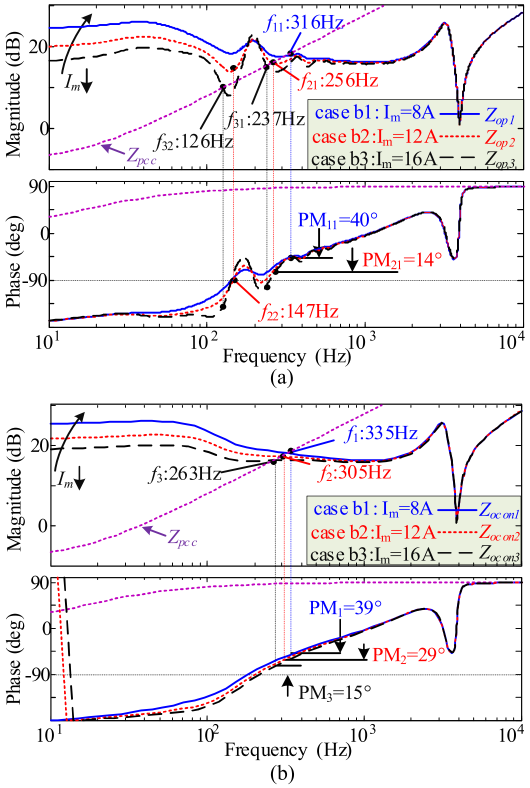

Fig. 15. Bode of $Z_{op}|_{Z\mathrm{pcc}}$ and $Z_{o-\mathrm{con}}$ under different I_m. ($f_b = 220$ Hz, SCR = 3.82). (a) Bode of $Z_{op}|_{Z\mathrm{pcc}}$ under different I_m. (b) Bode of $Z_{o-\mathrm{con}}$ under different I_m.

According to Figs. 15 and 16, the conclusions about the influence of PLL bandwidths and current references on the single-phase inverter-grid system stability can be made, i.e., the higher the PLL bandwidth or the current reference, the worse the system stability performance.

C. Influence of Number n on the Parallel System Stability

To figure out the influence of the number *n* on the parallel system stability, the output impedance of a three-parallel homogeneous-inverter system is studied. Two cases (case d: $I_{m1} = I_{m2} = I_{m3} = 12$ A and case e: $I_{m1} = 16$ A, $I_{m2} = 8$ A, $I_{m3} = 12$ A) are designed and plotted as the dashed line and the solid line in Fig. 17, respectively. The symbols Z_{oHN1d}, Z_{oHN2d}, Z_{oHN3d}, denote the output impedances of the parallel system of the case d when *n* is 1, 2, 3, respectively. The symbols Z_{oHN1e}, Z_{oHN2e}, Z_{oHN3e}, denote the output impedances of the parallel system of the case e when *n* is 1, 2, 3, respectively.

Two phenomena are found based on the output impedances of the *n*-parallel system in Fig. 17 with *n* increased from 1 to 3.

1) The output impedances of the two cases (case d and case e) are identical if the number *n* and the total grid current i_{tot} are the same, since the dashed line matches well with the solid line when *n* is 2 or 3 (see Z_{oHN2d} and Z_{oHN2e}, Z_{oHN3d}, and Z_{oHN3e}).

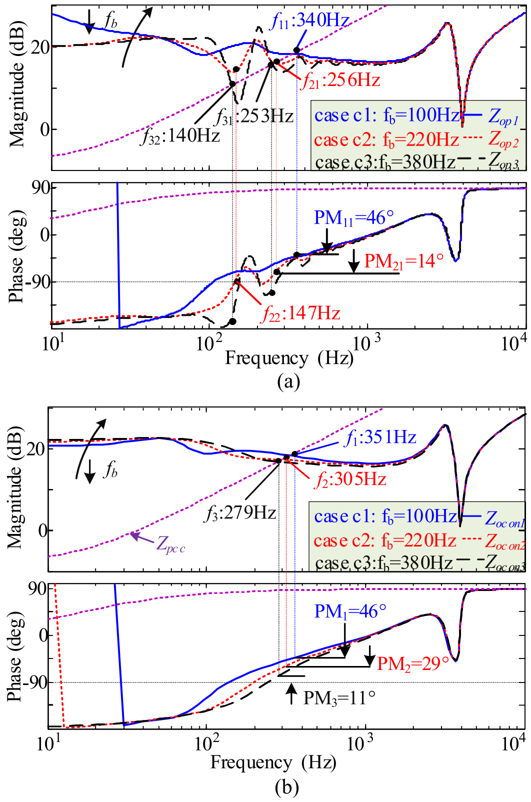

Fig. 16. Bode of $Z_{op}|_{Z\text{pcc}}$ and $Z_{o-\text{con}}$ under different f_b. ($I_m = 12$ A, SCR $= 3.82$). (a) Bode of $Z_{op}|_{Z\text{pcc}}$ under different f_b. (b) Bode of $Z_{o-\text{con}}$ under different f_b.

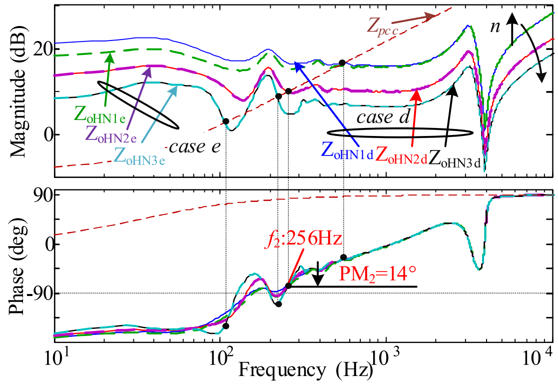

Fig. 17. Bode of $Z_{oHN}|_{Z\text{pcc}}$ with the number n increased from 1 to 3 ($L_{\text{pcc}} = 1.95$ mH, $f_b = 220$ Hz). Dashed-line: Case d, $I_{m1} = I_{m2} = I_{m3} = 12$ A, solid-line: Case e, $I_{m1} = 16$ A, $I_{m2} = 8$ A, $I_{m3} = 12$ A.

2) The n-parallel system stability is challenged by the increasing number, and the n-times amplification of the PCC impedance in the parallel system is satisfied only for one special inverter with the average grid current I_{avg}. In other words, the stability identified by $Z_{oHN}|_{Z\text{pcc}}/Z_{\text{pcc}}$ is equivalent to that identified by $Z_{op}|_{(n\cdot Z\text{pcc},I\text{avg})}/n \cdot Z_{\text{pcc}}$. For example, when $n = 2$, the PM corresponding to the intersected frequency 256 Hz of the magnitude-frequency curves Z_{oHN2d} and Z_{pcc} is 14° in Fig. 17, which is identical to the PM at the intersected frequency of Z_{op2} and Z_{pcc} in Fig. 14(a).

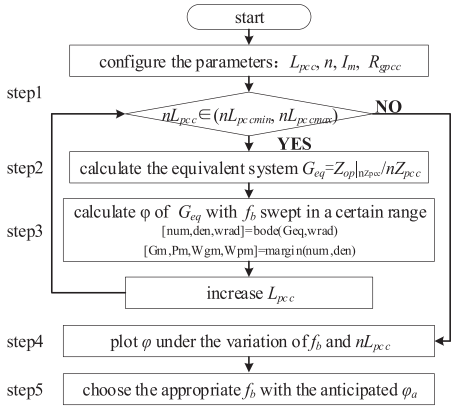

Fig. 18. Flowchart of the proposed design procedure of the bandwidth f_b.

The abovementioned two phenomena comply with the theoretical analyses in Section V-B.

VII. DESIGN GUIDELINE OF THE PLL BANDWIDTH

It is illustrated in Section VI that the stability of the single-phase grid-tied inverters is challenged by the PCC impedance Z_{pcc}, the current reference I_m, the number n, and the PLL bandwidth f_b. Since Z_{pcc} and n depends on the system configuration, and the inverter is required to operate stably under the full-load condition (i.e., I_m is set as the peak value of I_n), a probable way to guarantee the system stability under the weak grid is to optimize the selection of the PLL bandwidth f_b. Therefore, the design guideline of f_b with the anticipated PM φ_a is elaborated in this section, which is illustrated as a flowchart in Fig. 18.

Step 1: Configure the system parameters, $Z_{\text{pcc}} = sL_{\text{pcc}} + R_{\text{pcc}}$, n, I_m, and predefine the variation range of the PCC inductance as (L_{pccmin}, L_{pccmax}), wherein L_{pccmin} is used as the initialized value of L_{pcc}. If $n \cdot L_{\text{pcc}}$ belongs to the predefined impedance range, go to step 2. If not, step 4 is carried out.

Step 2: Derive the equivalent system G_{eq} (the impedance ratio of $Z_{op}|_{(n\cdot Z\text{pcc},Im)}/n \cdot Z_{\text{pcc}}$) in MATLAB.

Step 3: Calculate the PM φ of G_{eq} with f_b swept in a predefined frequency range. Increase L_{pcc} and go back to step 1.

Step 4: The graph of the PM φ versus to f_b and $n \cdot L_{\text{pcc}}$ is plotted as a 3-D figure.

Step 5: Choose the appropriate f_b from the graph based on the working condition of the inverter and the anticipated PM φ_a.

According to the design procedure of f_b, a design example is provided in Fig. 19, which illustrates the relationships among the inverter-grid system PM φ, the bandwidth f_b, and $n \cdot L_{\text{pcc}}$. The X, Y, Z axes are φ, nL_{pcc}, f_b, respectively. The contour line that φ equals 40° is also plotted and projected on the X-Y plane to give an intuitive illustration. In this case, three-parallel inverters whose parameters are provided in Table I are connected to the

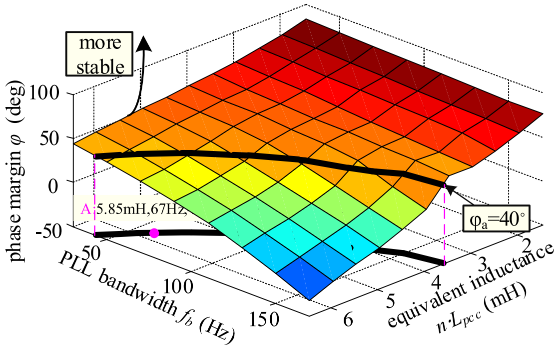

Fig. 19. Graphical illustration of φ under the variation of f_b and $n \cdot L_{\text{pcc}}$.

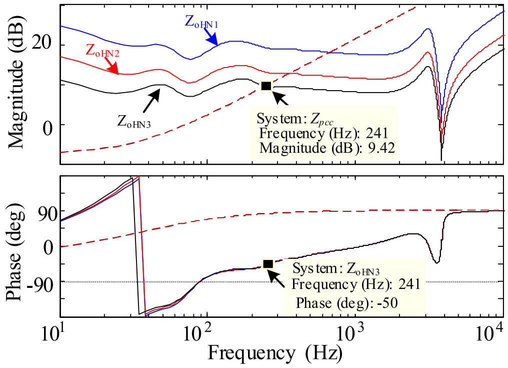

Fig. 20. Bode of $Z_{oHN}|_{Z\text{pcc}}$ with n increased from 1 to 3, ($I_m = 16$ A, $L_{\text{pcc}} = 1.95$ mH, $f_b = 67$ Hz).

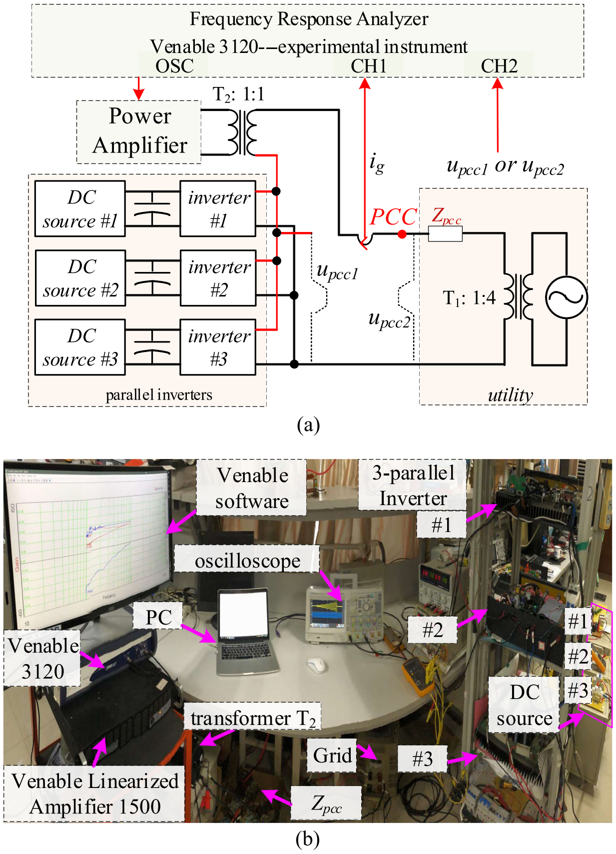

Fig. 21. Illustration of the experimental setup. (a) Circuit principle of the experimental setup. (b) Photograph of the experiment setup of the inverter-grid system.

grid with 1.95 mH + 0.4 Ω. By setting the anticipated PM φ_a as 40° ($n \cdot L_{\text{pcc}} = 5.85$ mH), the PLL bandwidth f_b is thereby chosen as 67 Hz based on the point A in Fig. 19. The output impedances of the 3-parallel system with n increased from 1 to 3 are plotted in Fig. 20 for verification. It is found that the PM is 40° when three inverters are paralleled to the grid, which complies with the design procedure.

VIII. EXPERIMENTAL VERIFICATIONS

A. Illustration of the Experimental Setup

To verify the correctness of the theoretical analyses and the proposed impedance model, experiments are conducted on a scaled-down multiparallel inverter system, whose parameters are listed in Table I. Fig. 21(a) shows the circuit configuration, where each inverter is independently controlled by the digital signal processor TMS320F28335. The input of the inverter is decoupled from the dedicated three-phase rectified dc source by the bulky electrolytic capacitors, and the output of the inverter are paralleled and connected to the utility through a stepup transformer T_1. The PCC impedance Z_{pcc} is lumped with the inserted inductor L_{ser} (for impedance modification) and the parasitic impedance of the transformer and the utility.

As shown in Fig. 21(a), the output impedance of the paralleled inverters is measured by sweeping the frequency of the injected small perturbance of the ac voltage source from 10 to 15 kHz, which is generated by the Venable Linear Amplifier VLA1500 together with the isolation transformer T_2. The sensed grid current i_g and the PCC voltage u_{pcc} are sent to the frequency response analyzer Venable 3120. Therefore, the ratio of u_{pcc1} to i_g is supposed to be the single-frequency output impedance, and the ratio of u_{pcc2} to $-i_g$ is deemed to be Z_{pcc}.

Fig. 21(b) shows the photograph of the experimental setup of 3-parallel single-phase grid-tied inverters. The experimental impedance results are recorded by the specialized Venable software and exported to the workspace of the MATLAB for comparing with the theoretical curves of $Z_{op}|_{(Z\text{pcc},\, Im)}$. The experimental waveforms are screened by the oscilloscope KeySight DSOX3024T.

B. Stability Verification with the PCC Impedance Variation

To reveal the influence of the PCC impedance on the stability of the single-phase grid-connected inverter in Section VI-A, Fig. 22(a)–(c) shows the waveforms of the inverter connected to different PCC impedances. The control parameters and Z_{pcc} are set to be consistent with the cases (case a1–a3) in Fig. 14. It is worth noting that large harmonics around 150 and 250 Hz (other than 305 Hz predicted by $Z_{o-\text{con}}$) are excited in the case a2 in Fig. 22(b), which is in accordance with the intersected frequency (f_{21}, f_{22}) of the gain curve of Z_{op2} and

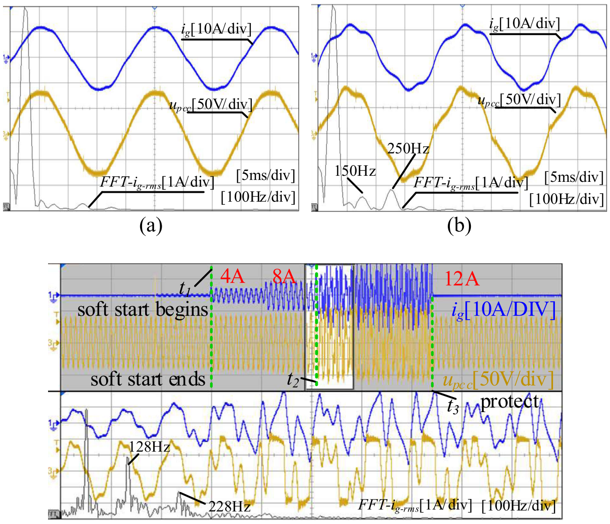

(a) (b)

(c)

Fig. 22. Waveforms of the inverter with varied Z_{pcc}, ($I_m = 12\,\text{A}$, $f_b = 220\,\text{Hz}$). (a) Case a1: $Z_{\text{pcc}} = 1.95\,\text{mH} + 0.4\,\Omega$. (b) Case a2: $Z_{\text{pcc}} = 3.85\,\text{mH} + 0.4\,\Omega$. (c) Case a3: $Z_{\text{pcc}} = 5.85\,\text{mH} + 0.4\,\Omega$.

Z_{pcc} in Fig. 14(a). Fig. 22(c) shows that the inverter-grid system turns unstable when Z_{pcc} further increases. When the inverter finishes the soft start at the instant t_2, the grid current starts to resonate severely and triggers the protection at t_3. The main resonant frequencies (128 Hz, 228 Hz) again match well with the intersected frequencies f_{31} and f_{32} in Fig. 14(a) and Table II.

Further on, to validate the developed output impedance model, the experimental measurements of the inverter output impedance in corresponding with case a1 and case a2 are recorded as Z_{op-m} (m means the measurement), and are marked with "o" in Fig. 23(a) and (b), respectively. As the case a3 in Fig. 14(c) is predicted to be unstable, it is hence impossible to measure the output impedance of the inverter, and is thereby not provided. From Fig. 23(a) and (b), it is found that Z_{op-m} matches well with theoretical curves Z_{op}, which validates the proposed impedance model described by (30). More importantly, the phenomenon that the output impedance depends not only on the inverter itself but also on the PCC impedance is verified, which means that attention should be paid to the impact of the FCE on the inverter output impedance.

C. Stability Verification with Different I_m and f_b

Fig. 24 shows the waveforms of the inverter with different current references in corresponding with the case b1 and case b3. It can be found that the quality of the grid current i_g in Fig. 24(a) is better than that of the case b2 (case a2, b2, c2 are the identical) in Fig. 22(b), since the amplitude of I_m is much lower in Fig. 24(a). When I_m is set as 1 p.u. in Fig. 24(b), the system diverges gradually from the instant t_2 (the soft start finishes), and finally the protection is triggered at t_3, which means that the case b3 in Fig. 15(a) is unstable, other than the stable case predicted by the impedance $Z_{o-\text{con}}$ in [27] and [28]. The resonant frequencies are also well predicted by Z_{op3} in Fig. 15(a).

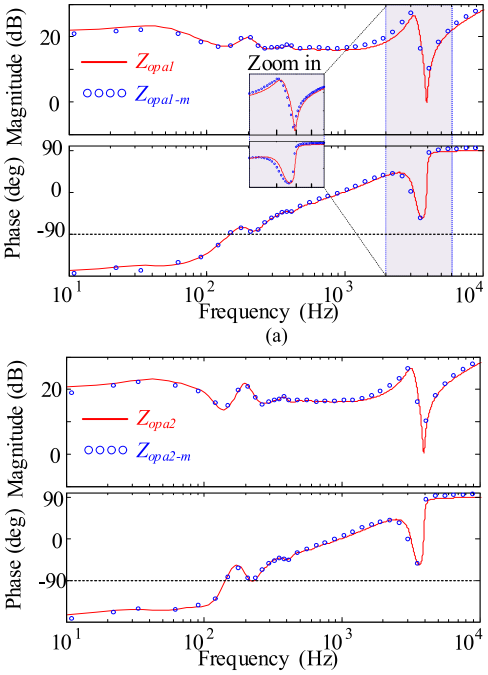

(a)

(b)

Fig. 23. Experimental measurement of the inverter output impedance under different grid impedance. (a) Case a1 in Fig. 14(a): $Z_{\text{pcc}} = 1.95\,\text{mH} + 0.4\,\Omega$. (b) Case a2 in Fig. 14(a): $Z_{\text{pcc}} = 3.85\,\text{mH} + 0.4\,\Omega$.

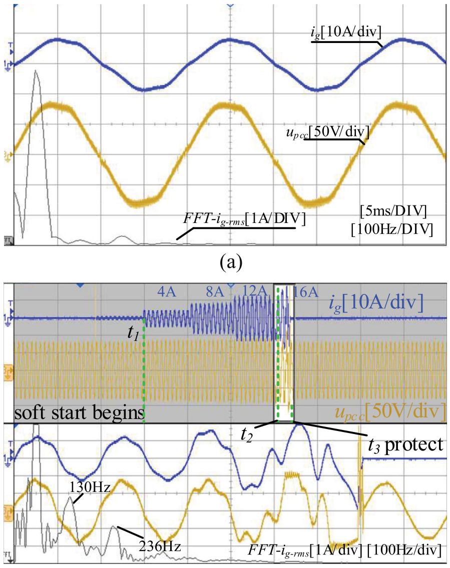

(a)

(b)

Fig. 24. Waveforms of the inverter with different I_m. $L_{\text{pcc}} = 3.85\,\text{mH}$. (a) $I_m = 8\,\text{A}$ (0.5 p.u.), $f_b = 220\,\text{Hz}$, case b1 in Fig. 15(a). (b) $I_m = 16\,\text{A}$ (1 p.u.), $f_b = 220\,\text{Hz}$, case b3 in Fig. 15(a).

Fig. 25 shows the waveforms of the inverter with different PLL bandwidths in corresponding with the case c1 and case c3. It can be found that the quality of the grid current i_g in Fig. 25(a) is better than that in Fig. 22(b), since the PLL bandwidth is lower. When the bandwidth increases to 380 Hz in Fig. 25(b), the system diverges gradually from the instant t_2 (the soft start

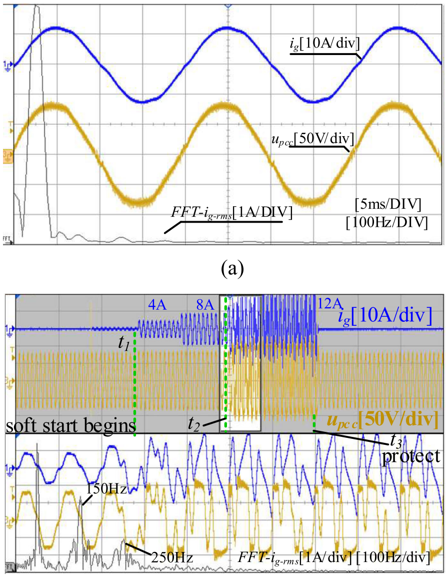

(a)

(b)

Fig. 25. Waveforms of the inverter with different f_b. $L_{\text{pcc}} = 3.85\,\text{mH}$. (a) $f_b = 100\,\text{Hz}$, $I_m = 12\,\text{A}$, case c1 in Fig. 16(a). (b) $f_b = 380\text{Hz}$, $I_m = 12\,\text{A}$, case c3 in Fig. 16(b).

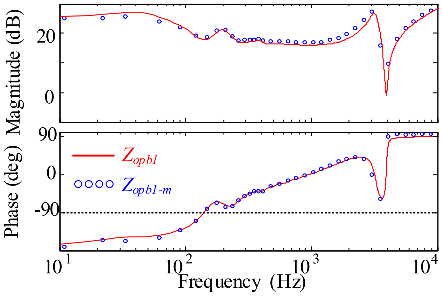

Fig. 26. Experimental measurement of the inverter output impedance with a lower current reference in Fig. 16(a) (case b1).

finishes), and finally the protection is triggered at t_3. The unstable case c3 is confirmed by the experimental waveform, and the dominant harmonics (150 Hz, 250 Hz) are indicated by Z_{op3} in Fig. 16(a).

Similarly, the measurement of the inverter output impedance in Figs. 24(a) and 25(a) are performed, and the results are marked with "o" in Figs. 26 and 27, respectively. It is observed that the theoretical curves match well with the experimental measurements, which again verifies the correctness of the proposed impedance model.

D. Stability Verification in 3-Parallel Systems

To verify the impedance model $Z_{oHN}|_{Z\text{pcc}}$ for the parallel system, experiments on a 3-parallel system are conducted.

Fig. 28(a) and (b) provides the waveforms of the parallel system of the case d and the case e in Fig. 17, respectively. First, both of the 3-parallel systems are stable when $n = 2$ ($i_{\text{tot}} = 24$ A), and unstable when $n = 3$ ($i_{\text{tot}} = 36$ A). Therefore, the conclusion that the characteristics of two systems are similar if the number and the total grid current are the same is experimentally verified. Second, the harmonic stability in Fig. 28 is similar to that in Fig. 22(c), and the stability of the parallel system with the increasing n is identical to the special inverter connected to the grid with $n \cdot Z_{\text{pcc}}$. Therefore, the conclusion in Section VI-C that the parallel system stability can be identified by $Z_{op}|_{(n\cdot Z\text{pcc},I\text{avg})}/n \cdot Z_{\text{pcc}}$ is verified.

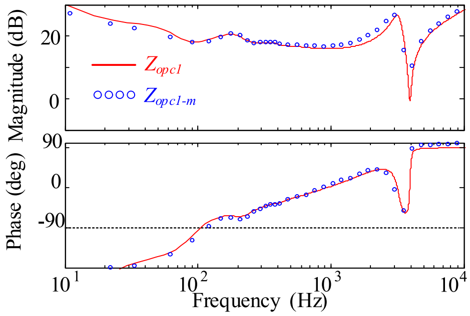

Fig. 27. Experimental measurement of the inverter output impedance with a lower bandwidth in Fig. 17(a) (case c1).

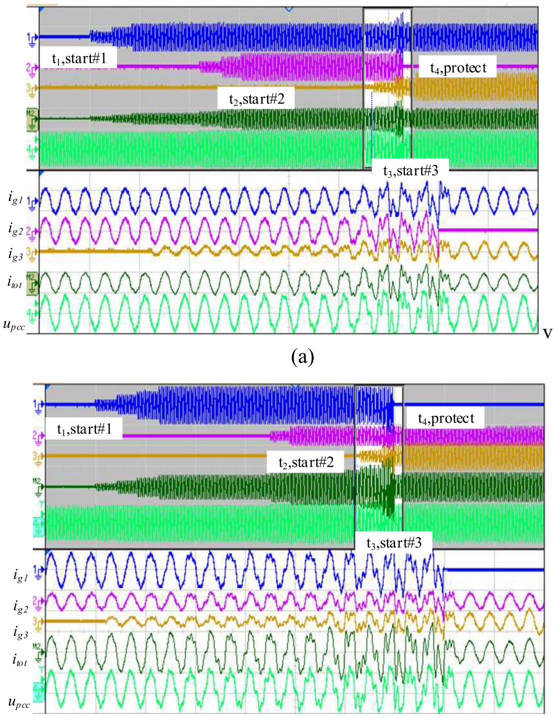

(a)

(b)

Fig. 28. Waveforms of 3-parallel system with different configurations of I_m. $f_b = 220\,\text{Hz}$, $Z_{\text{pcc}} = 1.95\,\text{mH} + 0.4\,\Omega$. (a) Case d in Fig. 17, $I_{m1} = I_{m2} = I_{m3} = 12\,\text{A}$. (b) Case e in Fig. 17, $I_{m1} = 16\,\text{A}$, $I_{m2} = 8\,\text{A}$, $I_{m3} = 12\,\text{A}$.

Fig. 29(a) and (b) further shows the experimental measurement of the output impedance for the two cases in Fig. 28(a) and (b), respectively. It is found that the impedance measurements match well with the theoretical curves of the proposed impedance model Z_{oHN}, which complies with the theoretical analysis in Section VI-C. The curves Z_{oHN-m} with $n = 2$ are similar in Fig. 29(a) and (b), which again verifies the conclusion

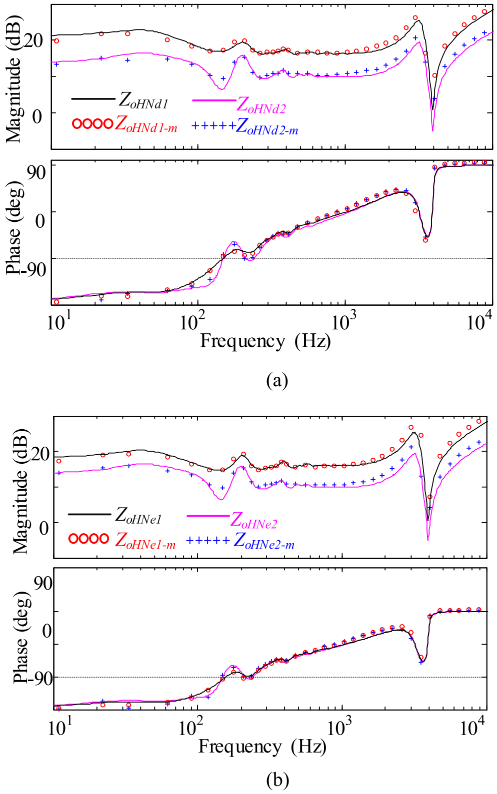

(a)

(b)

Fig. 29. Output impedance measurements of 3-parallel system with different configurations of I_m. (a) Case d in Fig. 17, $I_{m1} = I_{m2} = I_{m3} = 12\text{A}$. (b) Case e in Fig. 17, $I_{m1} = 16\,\text{A}$, $I_{m2} = 8\,\text{A}$, $I_{m3} = 12\,\text{A}$.

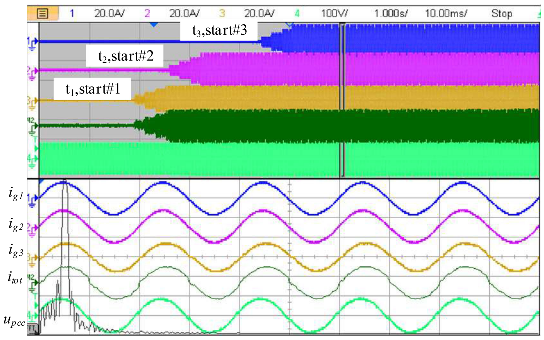

Fig. 30. Waveforms of 3-parallel system with the designed f_b. $f_b = 67\,\text{Hz}$, $Z_{\text{pcc}} = 1.95\,\text{mH} + 0.4\,\Omega$, $I_m = 16\,\text{A}$ (1.0 p.u.).

(a) in Section VI-C that the output impedances of two systems are identical if *n* and i_{tot} are the same.

To verify the correctness of the proposed design procedure of the bandwidth f_b in Section VII, the experimental waveforms of a three parallel system are shown in Fig. 30. It is found that the parallel system operates stably when the inverter is connected to the PCC one by one, and the total injected current i_{tot} keeps sinusoidal with the increasing *n*, which means that the selection of f_b is reasonable in the parallel system under the weak grid. Moreover, the output impedance of the 3-parallel system is measured, and it is shown in Fig. 31. It is found that the measurement result matches well with the theoretical curves with the increasing *n*, which again verifies the correctness of the proposed impedance model for the parallel system. Since the injected power is relatively high when $n = 3$, the perturbance gain of the Venable power amplifier needs to be decreased to avoid the overload operation at the frequencies lower than 100 Hz, which leads to slight difference between Z_{oHN-m} and Z_{oHN} in the frequency range 10–100 Hz.

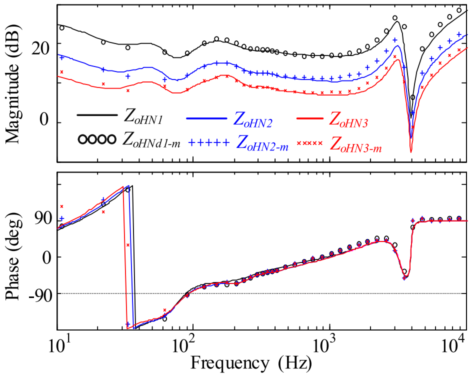

Fig. 31. Output impedance measurements of the 3-parallel system the designed f_b. $f_b = 67\,\text{Hz}$, $Z_{\text{pcc}} = 1.95\,\text{mH} + 0.4\,\Omega$, $I_m = 16\,\text{A}$ (1.0 p.u.).

IX. CONCLUSION

The output impedance modeling of the single-phase grid-tied inverters with capturing the FCE of the PLL is presented. A 3 × 3 MAM and a developed single-frequency output impedance are proposed to precisely assess the harmonic stability of the inverter-grid system. It is found that the FCE is contributed by the interactions between the PLL and the grid impedance, which may cause the inverter output impedance to vary along with the grid impedance. Extension of the proposed impedance model in the *n*-parallel inverter system reveals that the output impedances of two *n*-parallel homogeneous-inverter systems are identical if the number and the total injected current are the same, and the system stability is indicated by the ratio $\frac{1}{n} Z_{op}|_{(n \cdot Z_{\text{pcc}},\, I_{\text{avg}})} / Z_{\text{pcc}}$. Further on, the design procedure of the PLL bandwidth is elaborated, which guides the selection of the bandwidth with the anticipated PM. Analyses of the influence of different PCC impedances, PLL bandwidths, current references, and *n* have been performed with the proposed impedance model. The close correlations between the theoretical analyses and the experimental results verify that the correctness of the proposed impedance model and the design procedure of the PLL bandwidth. Synthesis of the dc dynamics of the dc-link voltage control to reveal the impedance behavior below the fundamental frequency needs further study.

REFERENCES

[1] F. Blaabjerg, Y. Yang, D. Yang, and X. Wasng, "Distributed power generation systems and protection," *Proc. IEEE*, vol. 105, no. 7, pp. 1311–1332, Jul. 2017.

[2] X. Wang and F. Blaabjerg, "Harmonic stability in power electronic based power systems: Concept, modeling, and analysis," *IEEE Trans. Smart Grid*, vol. 10, no. 3, pp. 2858–2870, May 2019, doi: 10.1109/TSG.2018.2812712.

[3] H. Bai, X. Wang, and F. Blaabjerg, "Passivity enhancement in renewable energy source based power plant with paralleled grid-connected VSIs," *IEEE Trans. Ind. Appl.*, vol. 53, no. 4, pp. 3793–3802, Apr. 2017.

[4] M. Lu, A. Al-Durra, S. M. Muyeen, S. Leng, P. C. Loh, and F. Blaabjerg, "Benchmarking of stability and robustness against grid impedance variation for LCL-filtered grid-interfacing inverters," *IEEE Trans. Power Electron.*, vol. 33, no. 10, pp. 9033–9046, Oct. 2018.

[5] A. Aapro, T. Messo, T. Roinila, and T. Suntio, "Effect of active damping on output impedance of three-phase grid-connected converter," *IEEE Trans. Ind. Electron.*, vol. 64, no. 9, pp. 7532–7541, Sep. 2017.

[6] M. Cespedes, "Impedance modeling, analysis, and adaptation of grid-connected inverters with PLL," Ph.D. dissertation, Dept. Elect. Comput. Syst. Eng., Rensselaer Polytechnic Inst., Troy, NY, USA, Nov. 2014.

[7] L. Harnefors, M. Bongiorno, and S. Lundberg, "Input-admittance calculation and shaping for controlled voltage-source converters," *IEEE Trans. Ind. Electron.*, vol. 54, no. 6, pp. 3323–3334, Jun. 2007.

[8] B. Wen, D. Dong, D. Boroyevich, R. Burgos, P. Mattavelli, and Z. Shen, "Impedance-based analysis of grid-synchronization stability for three-phase paralleled converters," *IEEE Trans. Power Electron.*, vol. 31, no. 1, pp. 26–38, Jan. 2016.

[9] Y. Liao, Z. Liu, H. Zhang, and B. Wen, "Low-frequency stability analysis of single-phase system with dq-frame impedance approach—Part II stability and frequency analysis," *IEEE Trans. Ind. Appl.*, vol. 54, no. 5, pp. 5012–5024, May 2018.

[10] C. Zhang, X. Wang, F. Blaabjerg, W. Wang, and C. Liu, "The influence of phase-locked loop on the stability of single-phase grid-connected inverter," in *Proc. IEEE Energy Convers. Congr. Expo.*, Montreal, Canada, 2015, pp. 4737–4744.

[11] Y. Han, M Luo, X. Zhao, J. Guerrero, and L. Xu, "Comparative performance evaluation of orthogonal signal generators based single-phase PLL algorithms—a survey," *IEEE Trans. Power Electron.*, vol. 31, no. 5, pp. 3932–3944, May 2016.

[12] M. G. Taul, X. Wang, P. Davari, and F. Blaabjerg, "Current reference generation based on next generation grid code requirements of grid-tied converters during asymmetrical faults," *IEEE J. Emerg. Sel. Topics Power Electron.*, to be published, doi: 10.1109/JESTPE.2019.2931725.

[13] Y. Yang, F. Blaabjerg, and Z. Zou, "Benchmarking of grid fault modes in single-phase grid-connected photovoltaic systems," *IEEE Trans. Ind. Appl.*, vol. 49, no. 5, pp. 2167–2176, Sep. 2013.

[14] H. A. Hamed, A. F. Abdou, E. Bayoumi, and E. Kholy, "A fast recovery technique for grid-connected converters after short dips using a hybrid structure PLL," *IEEE Trans. Ind. Electron.*, vol. 65, no. 4, pp. 3056–3068, Apr. 2018.

[15] D. Shin, K. Lee, J. Lee, D. Yoo, and H. Kim, "Implementation of fault ride-through techniques of grid-connected inverter for distributed energy resources with adaptive low-pass notch PLL," *IEEE Trans. Power. Electron.*, vol. 30, no. 5, pp. 2859–2871, May 2015.

[16] H. Berndt, M. Hermann, H. D. Kreye, R. Reinisch, U. Scherer, and J. Vanzetta, "Transmissioncode 2007–Network and system rules of the German transmission system operators," Verband der Netzbetreiber, Berlin, Germany, Tech. Rep., 2007. [Online]. Available: https://www.vde.com/resource/blob/937766/bfe325518ace878935966b6efbc493e4/transmissioncode-2007--network-and-system-rules-of-the-german-transmissionsystem-operators-data.pdf.

[17] H. Yi, X. Wang, F. Blaabjerg, and F. Zhuo, "Impedance analysis of SOGI-FLL-based grid synchronization," *IEEE Trans. Power Electron.*, vol. 32, no. 10, pp. 7409–7413, Oct. 2017.

[18] A. Rygg, M. Molinas, C. Zhang, and X. Cai, "On the equivalence and impact on stability of impedance modeling of power electronic converters in different domains," *IEEE J. Emerg. Sel. Topics Power Electron.*, vol. 5, no. 4, pp. 1444–1454, Apr. 2017.

[19] B. Wen, D. Boroyevich, R. Burgos, P. Mattavelli, and Z. Shen, "Analysis of D-Q small-signal impedance of grid-tied inverters," *IEEE Trans. Power Electron.*, vol. 31, no. 1, pp. 675–687, Jan. 2016.

[20] M. K. Bakhshizadeh *et al.*, "Couplings in phase domain impedance modelling of grid-connected converters," *IEEE Trans. Power Electron.*, vol. 31, no. 10, pp. 6792–6796, Dec. 2016.

[21] Y. Xu, L. Chen, and T. Zheng, "Frequency coupling characeristic modeling and stability analysis of doubly fed induction generator," *IEEE Trans. Energy Convers.*, vol. 33, no. 3, pp. 1475–1486, Mar. 2018.

[22] M. Cespedes and J. Sun, "Impedance modeling and analysis of grid-connected voltage-source converters," *IEEE Trans. Power Electron.*, vol. 29, no. 3, pp. 1254–1261, Mar. 2014.

[23] A. Rygg, M. Molinas, C. Zhang, and X. Cai, "A modified sequence-domain impedance definition and its equivalence to the dq-domain impedance definition for the stability analysis of AC power electronic systems," *IEEE J. Emerg. Sel. Topics Power Electron.*, vol. 4, no. 4, pp. 1383–1396, Dec. 2016.

[24] X. Li and H. X. Lin, "Multifrequency small-signal model of voltage source converters connected to a weak grid for stability analysis," in *Proc. IEEE Appl. Power Electron. Conf. Expo.*, Long Beach, CA, USA, 2016, pp. 728–732.

[25] X. Wang, L. Harnefors, and F. Blaabjerg, "Unified impedance model of grid-connected voltage-source converters," *IEEE Trans. Power Electron.*, vol. 33, no. 2, pp. 1775–1787, Feb. 2018.

[26] J. Sun, "Impedance-based stability criterion for grid-connected inverters," *IEEE Trans. Power Electron.*, vol. 26, no. 11, pp. 3075–3078, Nov. 2011.

[27] X. Chen, Y. Zhang, S. Wang, J. Chen, and C. Gong, "Impedance-phased dynamic control method for grid-connected inverters in a weak grid," *IEEE Tran. Power Electron.*, vol. 32, no. 1, pp. 274–283, Jan. 2017.

[28] C. Zhang, X. Wang, and F. Blaabjerg, "Analysis of phase-locked loop influence on the stability of single-phase grid-connected inverter," in *Proc. IEEE 6th Int. Symp. Power Electron. Distrib. Gener. Syst.*, Aachen, Germany, 2015, pp. 1–8.

[29] S. Lissandrom, L. D. Santa, and P. Mattavelli, "Experimental validation for impedance-based small-signal stability analysis of single-phase interconnected power systems with grid-feeding inverters," *IEEE J. Emerg. Sel. Topics Power Electron.*, vol. 4, no. 1, pp. 103–115, Mar. 2016.

[30] A. Sangwongwanich, Y. Yang, D. Sera, H. Soltani, and F. Blaabjerg, "Analysis and modeling of interharmonics from grid-connected photovoltaic systems," *IEEE Trans. Power Electron.*, vol. 33, no. 10, pp. 8353–8364, Oct. 2018.

[31] Y. Tang, F. Blaabjerg, and P. C. Loh, "A dual voltage control strategy for single-phase PWM converters with power decoupling function," *IEEE Trans. Power. Electron.*, vol. 30, no. 12, pp. 7060–7071, Dec. 2015.

[32] D. Yang, X. Wang, and F. Blaabjerg, "Sideband harmonic instability of paralleled inverters with asynchronous carriers," *IEEE Trans. Power Electron.*, vol. 33, no. 6, pp. 4571–4577, Jun. 2018.

[33] X. Yue, X. Wang, and F. Blaabjerg, "Review of small-signal modeling methods including frequency-coupling dynamics of power converters," *IEEE Trans. Power Electron.*, vol. 34, no. 4, pp. 3313–3328, Apr. 2019, doi: 10.1109/TPEL.2018.2848980.

[34] J. Lyu, X. Zhang, X. Cai, and M. Molinas, "Harmonic state-space based small-signal impedance modeling of a modular multilevel converter with consideration of internal harmonic dynamics," *IEEE Trans. Power Electron.*, vol. 34, no. 3, pp. 2134–2148, Mar. 2019.

[35] R. Turner, S. Walton, and R. Duke, "A case study on the application of the Nyquist stability criterion as applied to interconnected loads and sources on grids," *IEEE Trans. Ind. Appl.*, vol. 60, no. 7, pp. 2740–2749, Jul. 2013.

[36] T. Suntio, T. Messo, M. Berg, H. Alenius, and K. Zenger, "Impedance-based interactions in grid-tied three-phase inverters in renewable energy applications," *Energies*, vol. 12, no. 3, pp. 464–494, Mar. 2019.

Qiang Qian (S'15) was born in China, in 1992. He received the B.S. degree in electrical engineering from the Nanjing University of Aeronautics and Astronautics (NUAA), Nanjing, China, in 2012, where he is currently working toward the Ph.D. degree in power electronics.

His research interests include the modeling and the control of the multiparallel grid-connected inverters.

Shaojun Xie (M'05) was born in Hubei, China, in 1968. He received the B.S., the M.S., and the Ph.D. degrees in electrical engineering from the Nanjing University of Aeronautics and Astronautics (NUAA), Nanjing, China, in 1989, 1992, and 1995, respectively.

In 1992, he joined the Faculty of Electrical Engineering Teaching and Research Division, NUAA, where he is currently a Professor with the College of Automation Engineering. In recent five years, he has authored and coauthored over 100 technical papers published in many journals and international conference proceedings. His research interests include the aviation electrical power supply and power electronic conversion.

Dr. Xie was the recipient of the 2015 IET Power Electronics Premium Award.

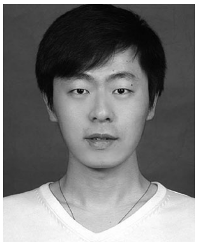

Jinming Xu (S'13–M'18) was born in Xuzhou, Jiangsu Province, China, in 1987. He received the B.S. degree in electrical engineering and the Ph.D. degree in power electronics from the Nanjing University of Aeronautics and Astronautics (NUAA), Nanjing, China, in 2009 and 2017, respectively.

In 2017, he joined the College of Automation Engineering, NUAA, where he is currently a Lecturer. He has authored and coauthored more than 50 technical papers in many international journals and conference proceedings. His research interests include the grid-connected inverters and control strategies, and renewable power generations.

Dr. Xu was the recipient of the 2015 IET Power Electronics Premium Award.

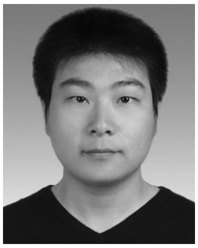

Kunshan Xu (M'17) was born in Lianyungang, China. He received the B.S. and M.S. degrees in automation from the Shandong University of Science and Technology, Qingdao, China, in 2007 and 2010, respectively, and the Ph.D. degree in electrical engineering from the Nanjing University of Aeronautics and Astronautics, Nanjing, China, in 2018.

In 2018, he joined the Nanjing Institute of Technology, where he is currently a Lecture. His current research interests mainly include modular multilevel converter and control technology of power electronic system.

Shenyiyang Bian was born in Jiangsu, China, in 1996. He received the B.S. degree in electrical engineering and automation, in 2018, from the Nanjing University of Aeronautics and Astronautics (NUAA), Nanjing, China, where he is currently working toward the M.S. degree in electrical engineering.

His research interests include the grid-connected inverters and control strategies.

Nini Zhong was born in Jiangsu Province, China, in 1996. She received the B.S. degree in electrical engineering in 2018 from the Nanjing University of Aeronautics and Astronautics (NUAA), Nanjing, China, where she is currently working toward the M.S. degree in electrical engineering.

Her research interests include the grid-connected inverters and control strategies.